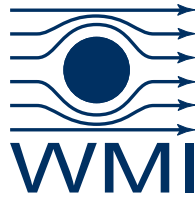




TECHNISCHE
UNIVERSITÄT
MÜNCHEN



WALTHER- MEISSNER-
INSTITUT FÜR TIEF-
TEMPERATURFORSCHUNG



BAYERISCHE
AKADEMIE DER
WISSENSCHAFTEN

Simulation of a Transmon Multibody Coupler for Lechner-Hauke-Zoller Quantum Annealing Architectures

Bachelor's Thesis

Aristo Kevin Ardyaneira P

Supervisor: Priv.-Doz. Dr. rer. nat. Frank Deppe
Garching, August 2021

Fakultät für Physik

TECHNISCHE UNIVERSITÄT MÜNCHEN

Contents

1	Introduction	1
2	Theory	4
2.1	Electrical Network Graph Theory	4
2.1.1	Fundamental Definitions of Graph Theory	4
2.1.2	Finding the Lagrangian	8
2.1.3	Eigenmodes of the linearized Josephson Circuit	9
2.1.4	Quantization and Truncation	10
2.2	Transmon Qubits	11
2.3	Josephson Ring Modulator	13
2.4	Quantum Annealing	16
2.5	Transmon Quantum Annealer	16
3	Results and Discussion	18
3.1	Deriving Circuit Hamiltonian	18
3.2	Quantum Annealing	23
3.2.1	Idealized Quantum Annealing	23
3.2.2	Parameters Fluctuations	31
3.2.3	Quantum Annealing with Dissipation	32
4	Summary and Outlook	38
	Bibliography	40

Chapter 1

Introduction

Quantum computation is a field of research which has been attracting more and more attention from scientists and engineers, as problems in science become more complicated over time. A quantum computer is a device for computation that takes advantage of phenomena existing only in quantum mechanics, such as superposition of states and quantum entanglement [1]. In contrast to a classical computer, where a memory consists of well-known bits, a quantum computer performs operations on quantum bits (qubits). A qubit is a quantum mechanical two-level system with the eigenstates $|0\rangle$ and $|1\rangle$ [1]. A qubit is thus in general described by the expression

$$|\psi\rangle = \alpha|0\rangle + \beta|1\rangle,$$

where α and β are complex coefficients and $|\alpha|^2$ ($|\beta|^2$) represents the probability to find the state $|0\rangle$ ($|1\rangle$) after measurement of $|\psi\rangle$. Due to this superposition, it is possible to store 2^n pieces of information with only n qubits, while in n classical bits only n pieces of information can be stored.

However, the implementation of a quantum computer is not without challenges. One unsolved problem in quantum computing is quantum decoherence, which results from the interaction of the qubit with its environment and causes information loss over time. There are several approaches aiming to build decoherence-resistant quantum computers. One of them is adiabatic quantum computation, which is theoretically predicted to be more robust against noise than other methods [2, 3, 4]. This prediction is attributed to the fact that in this approach, the ground state of a slowly evolving Hamiltonian is initially prepared and remains as the ground state throughout the evolution process [1, 5]. Since the system is always in the ground state, interaction with the environment cannot induce transitions to a lower state [1]. However, one must ensure that the temperature of the bath remains lower than the energy gap between the ground and the first excited state, such that thermal fluctuations cannot induce transitions to the higher states [1]. If this requirement is met, the state of final Hamiltonian will be in the ground state, in which the solution of the problem is encoded [5].

In all-to-all Ising spin glass formulation of adiabatic quantum annealing, the problem cost function is

cast into the form

$$H_f = \sum_{i=1}^N \sum_{j<i}^N J_{ij} \sigma_z^{(i)} \sigma_z^{(j)} + \sum_{i=1}^N b_i \sigma_z^{(i)}, \quad (1.1)$$

where $\sigma_z^{(i)}$ is the z -Pauli matrix associated with the i th spin. The interaction matrix J_{ij} and the additional local magnetic fields b_i fully parameterize the optimization problem [6]. The goal is to end up in the ground state of H_f by turning the classical spin variables into qubits and adiabatically transferring the system from a trivial initial state, for example the ground state of $H_0 = \sum_i h_i \sigma_x^{(i)}$, to H_f [6].

However, the spin-glass formulation of adiabatic quantum annealing is not without challenges. A fundamental challenge in this scheme is the required all-to-all connectivity [7, 8], while the natural qubit interactions only cover a finite range of values [9, 10]. Moreover, the possible quantum speedup due to the scaling of the minimal gap and the sensitivity of errors are still open fundamental questions [11, 12]. Recently, there is a proposal called parity adiabatic quantum optimization (PAQC) scheme aiming to address several of these challenges [6]. In this scheme, the logical qubits σ , which define the problem in Eq. (1.1), are redundantly encoded in the topology of a new architecture, enabling an intrinsic fault tolerance of the device [6]. To accommodate for all interaction matrix elements, the system size in this architecture is enlarged from N logical qubits to $K = N(N - 1)/2$ physical qubits $\tilde{\sigma}$ available in the laboratory. This increased number of degrees of freedom is compensated by $K - N + 1$ constraints C_l [6]. Thus, the optimization problem is encoded in the Hamiltonian [13]

$$H_p = \sum_{k=1}^K J_k \tilde{\sigma}_z^{(k)} + \sum_{l=1}^{K-N+1} C_l. \quad (1.2)$$

Lately, in the framework of superconducting qubits, a physical implementation of PAQC scheme has been suggested. The two-qubit building is based on Transmon qubits [13] and shown in Fig. 1.1.

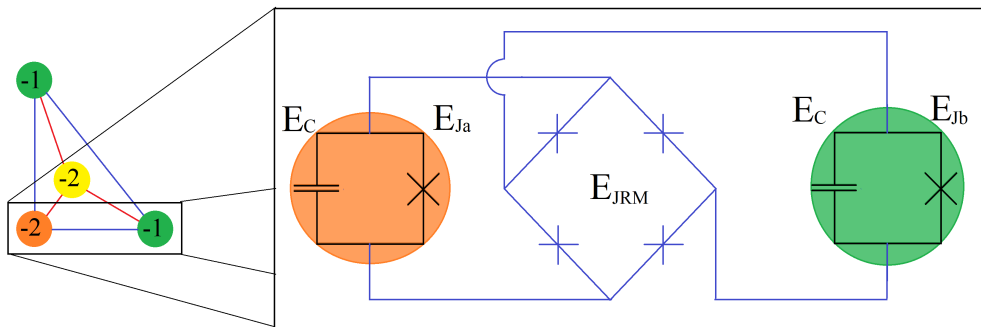


Figure 1.1: Illustration of the circuit diagram for the two-qubit building block of a quantum annealing processor based on Transmon qubit. As all interactions are assumed to be equal, this is the only required building block. Two Transmon qubits with charging energy E_C and Josephson energies E_{Ja} and E_{Jb} respectively are coupled by a Josephson ring modulator with Josephson energy E_{JRM} [13].

Hereby, the circuit incorporates Josephson ring modulators (JRM) to build Ising pair interactions that

are large compared to the onsite energies [13]. With a microwave drive, fully tunable longitudinal fields and transversal fields in a frame rotating with the microwave drive are introduced [13]. However, the behavior and the properties of this implementation have not been studied well yet and Leib omits the parasitic capacitance of Josephson junction in JRM [13], which, in turn, motivates this study. This thesis is structured as follows: In chapter 2, we review several theory aspects, which are essential for chapter 3. Our main focus is on the method of electrical network graph theory, which enables us to obtain the proper Hamiltonian for our circuit. Based on this theory, the derivation of Hamiltonian is presented in chapter 3. In this chapter, we first extract several important information from our Hamiltonian. Next, we study the behavior of our Hamiltonian during quantum annealing process both under idealized conditions and under consideration of jump operators.

Chapter 2

Theory

In order to derive the Hamiltonian of a relatively complex superconducting circuit, electrical network graph theory turns to be advantageous over the method of nodes [14]. Furthermore, our circuit consists of two Transmon qubits connected with a JRM, so we also review some important aspects of these circuit elements.

2.1 Electrical Network Graph Theory

Electrical network graph theory is a rigorous mathematical formalization of the Kirchhoff's current and voltage laws. As such, one can abstractly adapt it to graph theory based on these laws. The method to derive the Hamiltonian used in this thesis combines the methods of Rasmussen and Zlatko [14, 15]. Before we present the electrical network graph theory, it is indispensable that we review some fundamental definitions from graph theory, since the electrical network graph theory is built upon them. Here, all definitions are taken from Rasmussen [14].

2.1.1 Fundamental Definitions of Graph Theory

Definition 1 (Graph) A graph $\mathcal{G} = (\mathcal{N}, \mathcal{B})$ is a set of nodes $\mathcal{N} = \{n_1, \dots, n_N\}$, where N is the number of nodes, and a set of branches $\mathcal{B} = \{b_1, \dots, b_B\}$, where each branch connects a pair of nodes and B is the number of branches. The number of nodes is called the order of the graph and is denoted $|\mathcal{G}| = N$.

The very first step of any circuit analysis is to label every branch of the graph, usually via the flux flowing through each element $\Phi_i \equiv \int_{-\infty}^t V_i(t') dt'$. There are no specific conventions to label the branches and they can therefore be labeled in different ways [14].

Definition 2 (Subgraph) A graph $\mathcal{H} = (\mathcal{N}_{\mathcal{H}}, \mathcal{B}_{\mathcal{H}})$ is called a subgraph of $\mathcal{G} = (\mathcal{N}_{\mathcal{G}}, \mathcal{B}_{\mathcal{G}})$, written $\mathcal{H} \subseteq \mathcal{G}$, if $\mathcal{N}_{\mathcal{H}} \subseteq \mathcal{N}_{\mathcal{G}}$ and $\mathcal{B}_{\mathcal{H}} \subseteq \mathcal{B}_{\mathcal{G}}$. If \mathcal{H} is a subgraph of \mathcal{G} but $\mathcal{H} \neq \mathcal{G}$ it is called a proper subgraph.

With the definition of subgraphs, we can then define the spanning tree.

Definition 3 (Spanning tree) A spanning tree of a graph \mathcal{G} is a connected subgraph \mathcal{T} that contains the same nodes as \mathcal{G} and contains no loops. The branches of the spanning tree are called twigs and the branches of the complement of the spanning are called links. Note that there are $\mathcal{B}_{\mathcal{G}} - (N_{\mathcal{G}} - 1)$ links.

The noteworthy feature of spanning tree is that it connects every pair of nodes through exactly one path. From a physical point of view, the number of twigs corresponds to the maximum number of eigenmodes arising in the quantum system. Choosing a spanning tree allows us to define fundamental cutsets and fundamental loops.

Definition 4 (Cut) Given a graph $\mathcal{G} = (N, \mathcal{B})$ a cut is a partitioning of nodes N into two disjoint sets N_A and N_B . With every cut we can associate a cutset, which is the set of branches that have endpoints in both N_A and N_B .

Definition 5 (Fundamental cut) Given a graph \mathcal{G} and a spanning tree \mathcal{T} we define a fundamental cut or f -cut as a cut, whose cutset contains only one twig, yet any links.

Because per definition fundamental cutset only contains one twig, the total number of fundamental cutsets is always equal to the number of twigs of our circuit.

Definition 6 (Fundamental loop) Given a graph \mathcal{G} and a spanning tree \mathcal{T} we define a fundamental loop or f -loop as a loop consisting of exactly one link and one or more twigs.

The number of fundamental loop that can be formed is equal to the number of links of our circuit. Hence, the number of fundamental cuts and fundamental loops corresponds to the number of branches of our circuit.

Definition 7 (Fundamental loop matrix) Given a graph $\mathcal{G} = (N, \mathcal{B})$, with spanning tree \mathcal{T} , we define a fundamental loop matrix, or f -loop matrix, $F^{(L)}$ as

$$F_{ij}^{(L)} \equiv \begin{cases} +1 & \text{if } b_j \in f_i \text{ and } l_i, b_j \text{ have the same orientation,} \\ -1 & \text{if } b_j \in f_i \text{ and } l_i, b_j \text{ have the opposite orientation,} \\ 0 & \text{if } b_j \notin f_i, \end{cases}$$

where $1 \leq i \leq |\mathcal{B} \setminus \mathcal{T}| = B - (N - 1)$ and $1 \leq j \leq B$ and l_i is the link in the i th f -loop, f_i .

The definition 7 means nothing else than that we iterate through the branches and the set of f -loops. If the given branch is in the f -loop - which we consider, then the matrix entry becomes ± 1 . The entry takes the value $+1$, if the branch has the same orientation as the link contained in the f -loop and -1 , if it has the opposite orientation as the link. From the electrical circuit point of view, the fundamental loop matrix describes the Kirchhoff's voltage law.

Definition 8 (Fundamental cut matrix) Given a graph $\mathcal{G} = (N, \mathcal{B})$, with spanning tree \mathcal{T} , we define fundamental cut matrix, or f-cut matrix, $F^{(C)}$ as

$$F_{ij}^{(C)} \equiv \begin{cases} +1 & \text{if } b_j \in c_i \text{ and } t_i, b_j \text{ have the same orientation,} \\ -1 & \text{if } b_j \in c_i \text{ and } t_i, b_j \text{ have the opposite orientation,} \\ 0 & \text{if } b_j \notin c_i, \end{cases}$$

where $1 \leq i \leq |\mathcal{T}| = N - 1$ and $1 \leq j \leq B$ and t_i is the twig of the i th cutset, c_i .

Similar like definition 7, we iterate through the branches and the set of cutsets. If the given branch is in the given cutset, the matrix entry becomes ± 1 , with a plus if the branch has the same orientation as the twig. If the branch is not in the f-cutset, the matrix entry is 0. In contrast to fundamental loop matrix, fundamental cut matrix is based on Kirchhoff's current law.

Before we proceed to the next subsection, the calculation of f-cut matrix and f-loop matrix of charge qubits as illustrated in Fig. 2.1 is demonstrated as a concrete example. At first, the f-cutset as well as

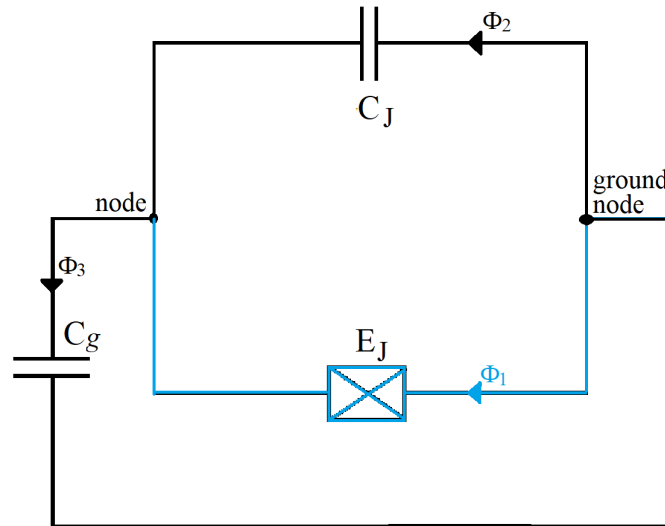


Figure 2.1: Circuit diagram of the single Cooper pair box without driving. The twig Φ_1 is marked with blue color of the branch. The cross denotes Josephson junction with Josephson energy E_J , while C_J and C_g represent parasitic and gate capacitance, respectively.

f-loop need to be determined. The f-cutset is simply the circuit itself, since it has only one twig, while the f-loop is depicted in Fig. 2.2. As the circuit only has one twig from three branches, the f-cut matrix has the dimension of $|\mathbf{F}^{(C)}| = 1 \times 3$ and is given by

$$\mathbf{F}^{(C)} = \begin{pmatrix} 1 & 1 & -1 \end{pmatrix},$$

where we conventionally use $+1$ for fluxes Φ_i going towards the node and -1 for fluxes going from

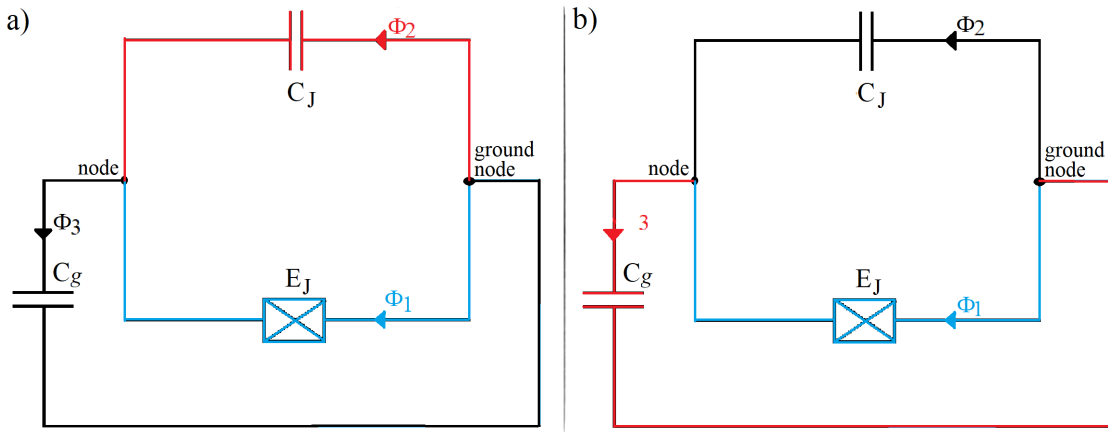


Figure 2.2: Fundamental loop of the circuit, which contains a) the first link Φ_2 and b) the second link Φ_3 .

the node. Subsequently, $F_{11}^{(C)}$ ($F_{12}^{(C)}$), which represents Φ_1 (Φ_2), takes the value $+1$, while $F_{13}^{(C)}$, which represents Φ_3 , takes -1 . Indeed, if we multiply f-cut matrix with the current vector $\mathbf{I} = (I_1, I_2, I_3)^T$ and equate to 0, we recover Kirchoff's current law. Next, we take a look in Fig. 2.2. Since there are two links from three branches, the f-loop matrix has the dimension of $|\mathbf{F}^{(L)}| = 2 \times 3$ and is provided by

$$\mathbf{F}^{(L)} = \begin{pmatrix} -1 & 1 & 0 \\ 1 & 0 & 1 \end{pmatrix},$$

where the first row of f-loop matrix $F_{1j}^{(L)}$ is based on Fig. 2.2a), whereas the second row $F_{2j}^{(L)}$ is based on Fig. 2.2b). All links rotate counterclockwise. As Φ_1 in Fig. 2.2a) flows clockwise, the entry $F_{11}^{(L)}$ takes the value -1 . The entry $F_{21}^{(L)}$ takes the value $+1$, since Φ_1 in Fig. 2.2b) flows counterclockwise. Analogously, as we multiply the f-loop matrix with the flux vector $\Phi = (\Phi_1, \Phi_2, \Phi_3)^T$, we find Kirchoff's voltage law.

Furthermore, one can easily verify that

$$\mathbf{F}^{(L)}(\mathbf{F}^{(C)})^T = \mathbf{0} \quad (2.1)$$

applies for the f-loop matrix and f-cut matrix of a single Cooper pair box. The Equation (2.1) is valid in general. This is attributed to the fact that the (i, j) th element depends only on the i th f-loop and the j th f-cut. If the f-cutset and f-loop share no branches, all the terms are zero, and in the case, where they share exactly two branches, we get two non-zero terms with opposite sign.

2.1.2 Finding the Lagrangian

The first step of deriving the Lagrangian of the circuit is to label the fluxes and currents flowing through all the circuit branches. In the method of Rasmussen [14], these are written as vectors

$$\Phi \equiv \begin{pmatrix} \Phi_t \\ \Phi_l \end{pmatrix}, \quad \mathbf{I} \equiv \begin{pmatrix} \mathbf{I}_t \\ \mathbf{I}_l \end{pmatrix}, \quad (2.2)$$

where Φ_t (\mathbf{I}_t) are the fluxes (currents) of all the twigs and Φ_l (\mathbf{I}_l) are the fluxes (currents) of all the links. The next step is defining the corresponding fundamental cut matrix as well as fundamental loop matrix according to definition 8 and 7. Expressing Kirchoff's laws of current and voltage in terms of this theory yields

$$\mathbf{F}^{(C)}\mathbf{I}(t) = 0, \quad \mathbf{F}^{(L)}\Phi(t) = \tilde{\Phi}(t) - \int_{-\infty}^t \mathbf{V}_V(t') dt', \quad (2.3)$$

where $\tilde{\Phi}^T = (\tilde{\Phi}_1, \dots, \tilde{\Phi}_{B-N+1})$ is the vector external fluxes through the fundamental loops and $(V_V)_i$ is the voltage generated by the source on the i th branch or 0, if the i th branch does not have a voltage source. Using Eq. (2.3), we can write the fluxes of our circuit without explicit dependence on the fluxes of the links

$$\Phi = (\mathbf{F}^{(C)})^{(T)}\Phi_t + \begin{pmatrix} 0 \\ \tilde{\Phi} - \int_{-\infty}^t \mathbf{V}_V(t') dt' \end{pmatrix}, \quad (2.4)$$

where the twigs of the circuit are chosen in the way that they do not include any voltage source.

Under the assumption that the circuit does not contain any linear inductance, the Lagrangian of our circuit is given by

$$\begin{aligned} \mathcal{L} = & \frac{1}{2} \dot{\Phi}_t^T \mathbf{C} \dot{\Phi}_t + \mathbf{Q}_0 \cdot \dot{\Phi}_t \\ & + \mathbf{E}_J \cdot \left(\cos \left((\mathbf{F}^{(C)})^{(T)} \frac{\Phi_t}{\Phi_0} + \begin{pmatrix} 0 \\ \tilde{\Phi} - \int_{-\infty}^t \mathbf{V}_V(t') dt' \end{pmatrix} \cdot \frac{1}{\Phi_0} \right) - \mathbf{1} \right), \end{aligned} \quad (2.5)$$

where

$$\mathbf{C} \equiv \mathbf{F}^{(C)} \mathbf{D}_C (\mathbf{F}^{(C)})^T \quad (2.6)$$

is the capacitance matrix with diagonal matrix \mathbf{D}_C , whose matrix entries are circuit capacitances, and

$$\mathbf{Q}_0 \equiv \mathbf{F}^{(C)} \mathbf{D}_C \begin{pmatrix} 0 \\ \dot{\tilde{\Phi}} \end{pmatrix} \quad (2.7)$$

are the offset charges. Furthermore, \mathbf{E}_J is the vector of Josephson energy, whose entries take the value of corresponding Josephson energy. $\Phi_0 \equiv \hbar/(2e)$ is the reduced magnetic flux quantum and $\mathbf{1}$ is simply a vector $(1, \dots, 1)^T$ with the dimension of the total number of circuit branches. Similarly, the cosine term in Eq. (2.5) means a vector $(\cos(\phi_1), \dots, \cos(\phi_N))^T$ with the same dimension. The Φ_i -entries are equal to

the i th-element of $(\mathbf{F}^{(C)})^{(T)} \Phi_t / \Phi_0 + (0, \check{\Phi} / \Phi_0 - \int_{-\infty}^t \mathbf{V}_V(t') / \Phi_0 dt')$.

2.1.3 Eigenmodes of the linearized Josephson Circuit

In principle, one can find the Hamiltonian of the circuit by performing a Legendre transformation on the Eq. (2.5). One might, however, be interested in the eigenmodes of the circuit and change to the associated eigenbasis, as this can be used to control unwanted couplings between modes [14]. This approach is useful for implementing a system with direct and thus strong multibody interactions [16], like four-body couplings, which are necessary for quantum annealing. There are as such many proposals for their implementation, though the interaction is a higher-order interaction, which is not directly visible in the first-order Hamiltonian. Such indirect interactions are generally slower and noisier, as they consist of multiple subprocesses [14]. For this reason, the Lagrangian needs to be diagonalized first. Hence, one separates the linear part of Lagrangian, which consists of the capacitive and linear inductive parts, from the non-linear part, which arises due to the Josephson terms. The diagonalization is then performed on the linear part, leaving the non-linear part undiagonalized. Later, the non-linear part is expressed in the newly attained basis. The method presented here is all based on Mineev [15].

The inductance matrix \mathbf{L}^{-1} of the circuit is a positive-definite, real, symmetric (PDRS) matrix, so that it can be diagonalized with a real orthogonal matrix \mathbf{O}_L . This procedure yields

$$\mathcal{L}_{\text{linear}} = \frac{1}{2} \dot{\Phi}_t^T \mathbf{C} \dot{\Phi}_t - \frac{1}{2} (\Phi_t^T \mathbf{O}_L \Lambda_L^{-1/2}) \mathbf{I}_L^{-1} (\Phi_t^T \mathbf{O}_L \Lambda_L^{-1/2})^T, \quad (2.8)$$

where $\Lambda_L^{-1/2}$ is the square-root of the diagonalized \mathbf{L}^{-1} and \mathbf{I}_L^{-1} is an identity matrix with the physical dimension of inductance. By defining

$$\check{\Phi} \equiv \Lambda_L^{-1/2} \mathbf{O}_L^T \Phi_t, \quad (2.9)$$

where $\check{\mathbf{C}} \equiv (\Lambda_L^{1/2} \mathbf{O}_L^T) \mathbf{C} (\Lambda_L^{1/2} \mathbf{O}_L^T)^T$ is a transformed capacitance matrix, which is positive-definite, real, and symmetric. For this reason, $\check{\mathbf{C}}$ can be diagonalized using a real orthogonal matrix $\mathbf{O}_{\check{\mathbf{C}}}$. By defining

$$\Phi_m \equiv \mathbf{O}_{\check{\mathbf{C}}}^T \check{\Phi} \quad (2.10)$$

the Lagrangian is finally diagonalized as follows

$$\tilde{\mathcal{L}}_{\text{linear}} = \frac{1}{2} \dot{\Phi}_m^T \Lambda_{\check{\mathbf{C}}} \mathbf{I}_C \dot{\Phi}_m - \frac{1}{2} \Phi_m^T \mathbf{I}_L^{-1} \Phi_m, \quad (2.11)$$

where $\Lambda_{\check{\mathbf{C}}}$ is the diagonal form of $\check{\mathbf{C}}$ and \mathbf{I}_C is an identity matrix with physical dimension of a capacitance. To obtain the full Lagrangian, one simply adds non-linear part $\tilde{\mathcal{L}}_{\text{nl}}$ to the linear part $\tilde{\mathcal{L}}_{\text{linear}}$, where the non-linear part $\tilde{\mathcal{L}}_{\text{nl}}$ needs to be expressed in terms of the new basis, which is related to the

old basis via

$$\Phi_t = \mathbf{E}\Phi_m, \quad \mathbf{E} \equiv \mathbf{O}_L \Lambda_L^{1/2} \mathbf{O}_{\check{c}}. \quad (2.12)$$

After the diagonalization process, a Legendre transformation provides the Hamiltonian

$$\mathcal{H} = \frac{1}{2} \mathbf{Q}_m^T \Omega^2 \mathbf{I}_L \mathbf{Q}_m + \frac{1}{2} \Phi_m^T \mathbf{I}_L^{-1} \Phi_m - \tilde{\mathcal{L}}_{\text{nl}}, \quad (2.13)$$

where

$$\Omega \equiv \Lambda_{\check{c}}^{-1/2} \mathbf{I}_\omega = \text{diag}(\omega_1, \dots, \omega_M) \quad (2.14)$$

is the diagonal eigenfrequency matrix of the linear Hamiltonian $\mathcal{H}_{\text{linear}}$, into which the linear Lagrangian transforms after the Legendre transformation.

2.1.4 Quantization and Truncation

After the diagonalization process, the full Hamiltonian is now ready to be quantized. The quantization procedure works similar as for a quantum mechanical harmonic oscillator. That is, we introduce the annihilation operator [15]

$$\hat{\mathbf{a}}(t) \equiv \frac{1}{\sqrt{2\hbar\Omega}} (\Phi_m(t) \mathbf{1}_H^{-1/2} + i\Omega \mathbf{Q}_m(t) \mathbf{1}_H^{1/2}), \quad (2.15)$$

which is equivalent to the following substitution [15]

$$\hat{\Phi}_m \equiv \sqrt{\frac{\hbar}{2}} \Omega^{1/2} \mathbf{I}_{H^{1/2}} (\hat{\mathbf{a}}^\dagger + \hat{\mathbf{a}}), \quad \hat{\mathbf{Q}}_m \equiv i \sqrt{\frac{\hbar}{2}} \Omega^{-1/2} \mathbf{I}_{H^{-1/2}} (\hat{\mathbf{a}}^\dagger - \hat{\mathbf{a}}). \quad (2.16)$$

The next and final step of deriving the Hamiltonian of our circuit is to truncate the Hamiltonian into n -energy levels. Assuming that during the whole annealing process the circuit is not provided with the energy greater than the difference between the first E_1 and the second E_2 eigenenergy, it is actually sufficient to truncate the Hamiltonian to two lowest states. These states are ground state $|0\rangle$ and first excited state $|1\rangle$. Together, those two states form a two-level quantum mechanical system, which is called qubit and on which a quantum annealer performs operations. The two-level truncation of the several possible combinations of creation and annihilation operators can be seen in table 2.1.

In reality, however, it is highly likely, that the noise from the environment might excite transitions from the first excited to the second excited state, so that truncating to more than two levels is necessary. In this case, the matrix entries of Hamiltonian terms $\hat{\mathcal{M}}$ can be found through $\hat{\mathcal{M}}_{ij} = \langle i | \hat{\mathcal{M}} | j \rangle$.

There is an optional step prior to truncation, which is the rotating wave approximation. The idea of this approximation is to neglect all terms, which in the interaction picture rotate very fast. In order to carry out this approximation, one needs to split the quantized Hamiltonian into the free part $\hat{\mathcal{H}}_0$ and the interaction part $\hat{\mathcal{H}}_{I,S}$. The linear quantized Hamiltonian is usually chosen as the free part, whereas

Step operators	Pauli operators
$\hat{a}^\dagger - \hat{a}$	$-i\sigma^y$
$\hat{a}^\dagger + \hat{a}$	σ^x
$(\hat{a}^\dagger + \hat{a})^3$	$3\sigma^x$
$(\hat{a}^\dagger + \hat{a})^4$	$-6\sigma^z$
$(\hat{a}_i^\dagger - \hat{a}_i)(\hat{a}_j^\dagger - \hat{a}_j)$	$-\sigma_i^x \sigma_j^x$
$(\hat{a}_i^\dagger + \hat{a}_i)(\hat{a}_j^\dagger + \hat{a}_j)$	$\sigma_i^x \sigma_j^x$
$(\hat{a}_i^\dagger + \hat{a}_i)^3(\hat{a}_j^\dagger + \hat{a}_j)$	$3\sigma_i^x \sigma_j^x$
$(\hat{a}_i^\dagger + \hat{a}_i)^2(\hat{a}_j^\dagger + \hat{a}_j)^2$	$\sigma_i^z \sigma_j^z - 2\sigma_i^z - 2\sigma_j^z$

Table 2.1: Overview of the different combinations of the step operators and their truncation to two dimensional Pauli operators. Subscripts are included for the interaction terms, and refer to different nodes. All constant terms have been neglected [14].

the rest is treated as interaction part. By transforming into the frame \mathcal{H}_0 as follows, [14]

$$\hat{\mathcal{H}} \rightarrow \hat{\mathcal{H}}_R = \hat{\mathcal{U}}(t)^\dagger \hat{\mathcal{H}} \hat{\mathcal{U}}(t) + i \frac{\partial \hat{\mathcal{U}}(t)^\dagger}{\partial t} \mathcal{U}(t), \quad (2.17)$$

where $\hat{\mathcal{U}}(t) \equiv \exp(-i\hat{\mathcal{H}}_0 t)$. Frequently, one can then neglect all terms proportional to $\exp(i\omega t)$, if ω is sufficiently larger than the term coefficients [14].

This approximation is, however, not performed in our work, since the time evolution of the Hamiltonian is studied numerically.

2.2 Transmon Qubits

Among superconducting qubits, Transmon qubits are a leading platform with respect to energy relaxation and dephasing times [17, 18, 19, 20]. They have a strong resilience to the ubiquitous charge noise in any superconducting qubit devices [13]. This resilience stems from the fact that the charge dispersion flattens exponentially in E_J/E_C , while the anharmonicity only decreases algebraically in E_J/E_C [14]. To reach higher E_J/E_C ratio, a large shunting capacitance C_B is often installed in parallel to the Josephson junction with Josephson energy E_J and parasitic capacitance C_J [14]. The circuit can be seen in Fig. 2.3. Due to the shunting capacitor, the effective capacitive energy becomes

$$E_C = \frac{e^2}{2(C_J + C_B + C_g)}, \quad (2.18)$$

which gives us much more freedom in choosing the ratio E_J/E_C and we can thus solve the Hamiltonian for the energy dispersion for larger E_J/E_C [14].

Using electrical network graph theory, one can show that the behavior of Transmon qubit can be

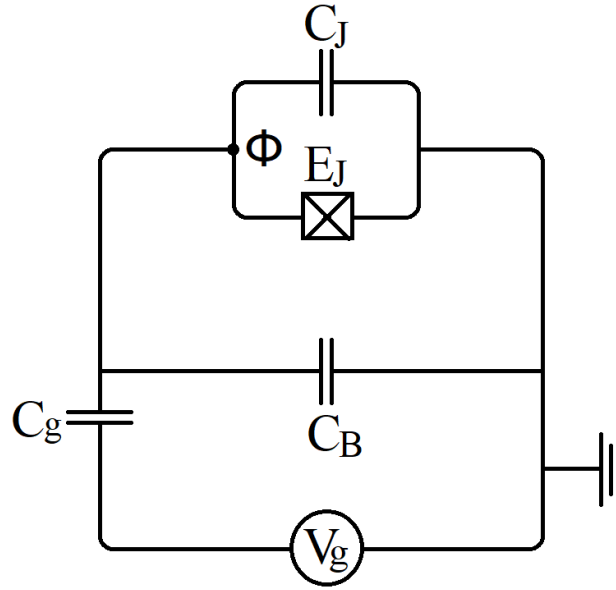


Figure 2.3: Circuit diagram of the Transmon qubit, consisting of a Josephson junction - with energy E_J and parasitic capacitance C_J , in series with a capacitor of capacitance C_g . The Josephson junction is shunted by a large capacitance, C_B [14].

described by the quantized Hamiltonian

$$\hat{\mathcal{H}} = 4E_C(\hat{n} - \hat{n}_g)^2 - E_J \cos(\hat{\Phi}) = 4E_C \sum_{n=-\infty}^{\infty} (n - n_g)^2 |n\rangle\langle n| - \frac{E_J}{2} \sum_{n=-\infty}^{\infty} (|n\rangle\langle n+1| + \text{h.c.}), \quad (2.19)$$

where $\hat{n}_g \equiv C_g V_g / 2e$ is the offset charge [14]. The plot of the lowest lying states of the Transmon qubit as a function of the offset charge n_g can be seen in Fig. 2.4.

Without Josephson energy ($E_J/E_C = 0$), the energy spectrum of the system is a set of parabolas when plotted against n_g , one for each eigenvalue of \hat{n} . The parabolas cross at $n_g = n + 1/2$, where $n \in \mathbb{Z}$, see Fig. 2.4(a). We notice that the states $|n\rangle$ and $|n+1\rangle$ are degenerate at $n_g = n + 1/2$.

Introducing the Josephson junction lifts the degeneracy, thus making an avoided crossing at $n_g = n + 1/2$, see Fig. 2.4(b)-(d). The distance between these avoided crossings is approximately equal to the Josephson junction energy E_J for the lowest states in the spectrum [14]. It is also noticeable that the steepness of the energy dispersion around the working point $n_g = n + 1/2$ is inversely related to the ratio E_J/E_C . This explains, why the large E_J/E_C ratio of Transmon qubit helps reducing its sensitivity to small fluctuations of the gate voltage V_g , as this gate voltage changes n_g . Since the eigenstates of the Transmon qubit are characterized by small zero-point fluctuations, it is appropriate to truncate the Josephson energy, which is given by the cosine of the phase, to fourth order [13]

$$\hat{\mathcal{H}} = 4E_C(\hat{n} - \hat{n}_g)^2 - E_J \cos(\hat{\Phi}) \approx 4E_C(\hat{n} - \hat{n}_g)^2 - E_J + E_J \frac{\hat{\Phi}^2}{2} - E_J \frac{\hat{\Phi}^4}{24}, \quad (2.20)$$

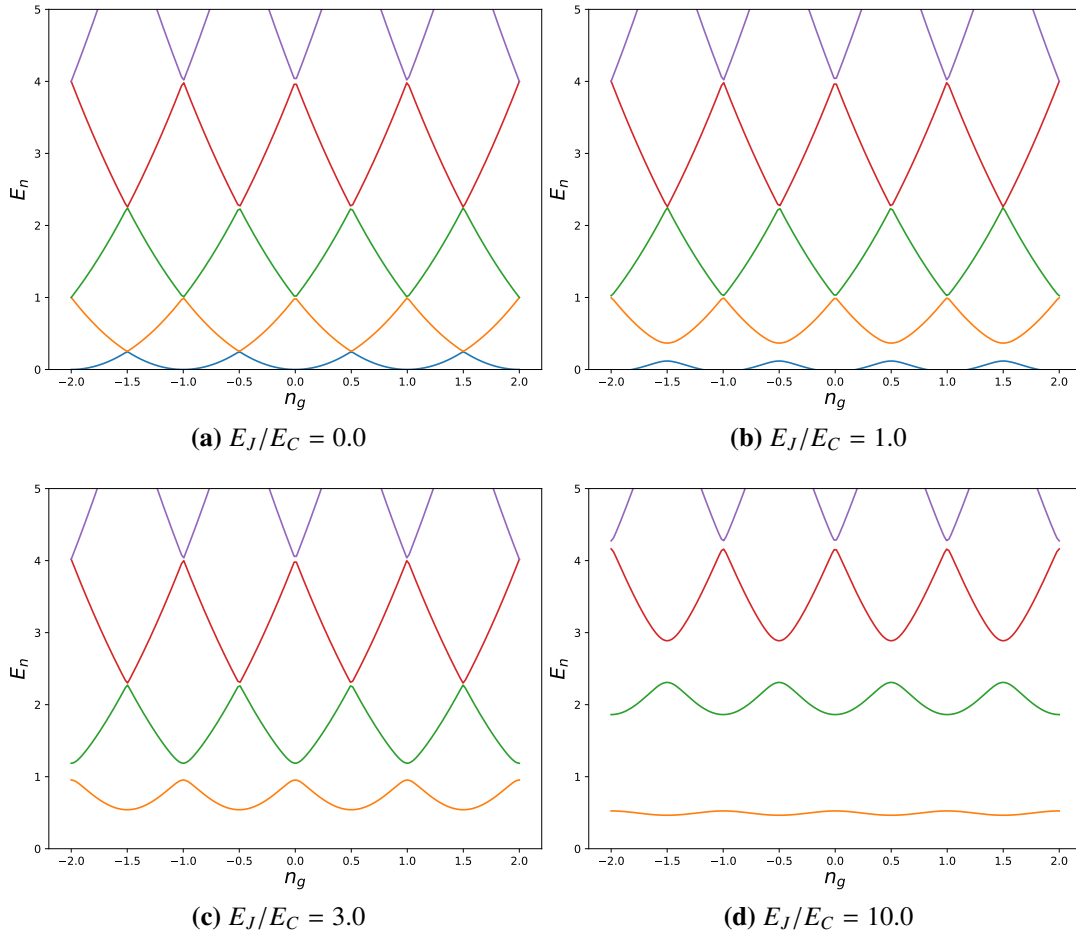


Figure 2.4: The energies of the lowest lying states of the Transmon qubit as a function of the offset charge n_g .

which, with the help of rotating wave approximation, becomes

$$4E_C(\hat{n} - \hat{n}_g)^2 - E_J + E_J \frac{\hat{\Phi}^2}{2} - E_J \frac{\hat{\Phi}^4}{24} \approx \sqrt{8E_J E_C} a^\dagger a - \frac{E_C}{2} a^\dagger a^\dagger a a. \quad (2.21)$$

2.3 Josephson Ring Modulator

In several cases, one wants to build a circuit, where its qubits can interact with each other. The smallest example of multibody interaction must consist of four nodes, as we can always decouple the center-of-mass-node leaving three true degrees of freedom [14]. An example for a circuit, which can be used to couple several qubits, is Josephson ring modulator (JRM) depicted in Fig. 2.5. The symbol φ_i denotes the nodes of the circuit and is not to be mistaken with Φ_i , which denotes the fluxes of the circuit.

We consider the case that $C_{\text{JRM},i} = C_J$ for $i \in \{1,2,3,4\}$. The capacitance matrix describing the circuit in

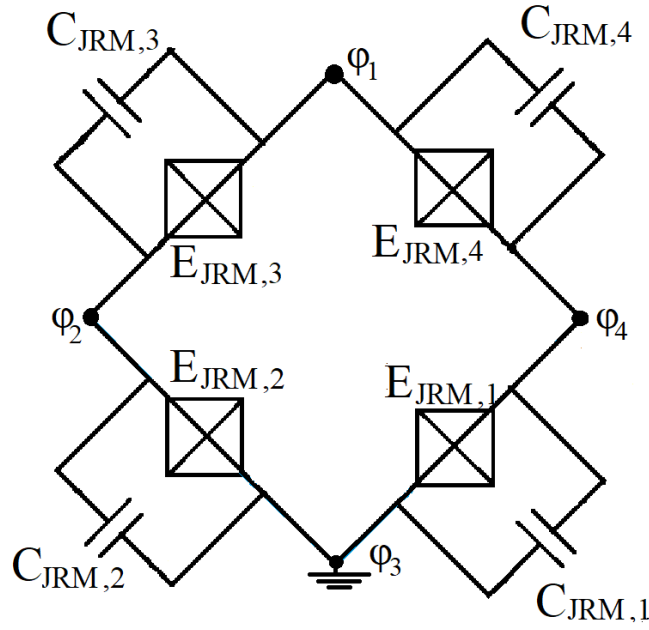


Figure 2.5: Circuit diagram of the JRM with four nodes φ .

Fig. 2.5 is given by

$$\mathbf{C} = \begin{pmatrix} 2C_{JRM} + C_J & -C_{JRM} & -C_J & -C_{JRM} \\ -C_{JRM} & 2C_{JRM} & -C_{JRM} & 0 \\ -C_J & -C_{JRM} & 2C_{JRM} + C_J & -C_{JRM} \\ -C_{JRM} & 0 & -C_{JRM} & 2C_{JRM} \end{pmatrix},$$

which after diagonalization yields the modes

$$\begin{aligned} \mathbf{v}_{CM} &= \frac{1}{2}(1,1,1,1)^T, & \mathbf{v}_1 &= \frac{1}{2}(1,0,-1,0)^T \\ \mathbf{v}_2 &= \frac{1}{2}(0,1,0,-1)^T, & \mathbf{v}_3 &= \frac{1}{2}(1,-1,1,-1)^T, \end{aligned}$$

with eigenvalues $\lambda_{CM} = 0$, $\lambda_1 = \lambda_3 = 4C$, and $\lambda_2 = 2C$ [14]. These modes correspond to charge oscillating between nodes 1 and 3 (\mathbf{v}_1), between nodes 2 and 4 (\mathbf{v}_2), and charge oscillations involving the nodes 1 and 3 as well as the nodes 2 and 4 (\mathbf{v}_3) [14],[21].

Later, we denote \mathbf{v}_1 as Y-eigenmode, \mathbf{v}_2 as X-eigenmode, and \mathbf{v}_3 as Z-eigenmode. Now, if the capacitance matrix \mathbf{C} is diagonalized, one attains the diagonalized form as follows [14]

$$\mathbf{K} = \begin{pmatrix} 0 & 0 & 0 & 0 \\ 0 & 2(C_{JRM} + C_J) & 0 & 0 \\ 0 & 0 & 2C & 0 \\ 0 & 0 & 0 & 4C \end{pmatrix}$$

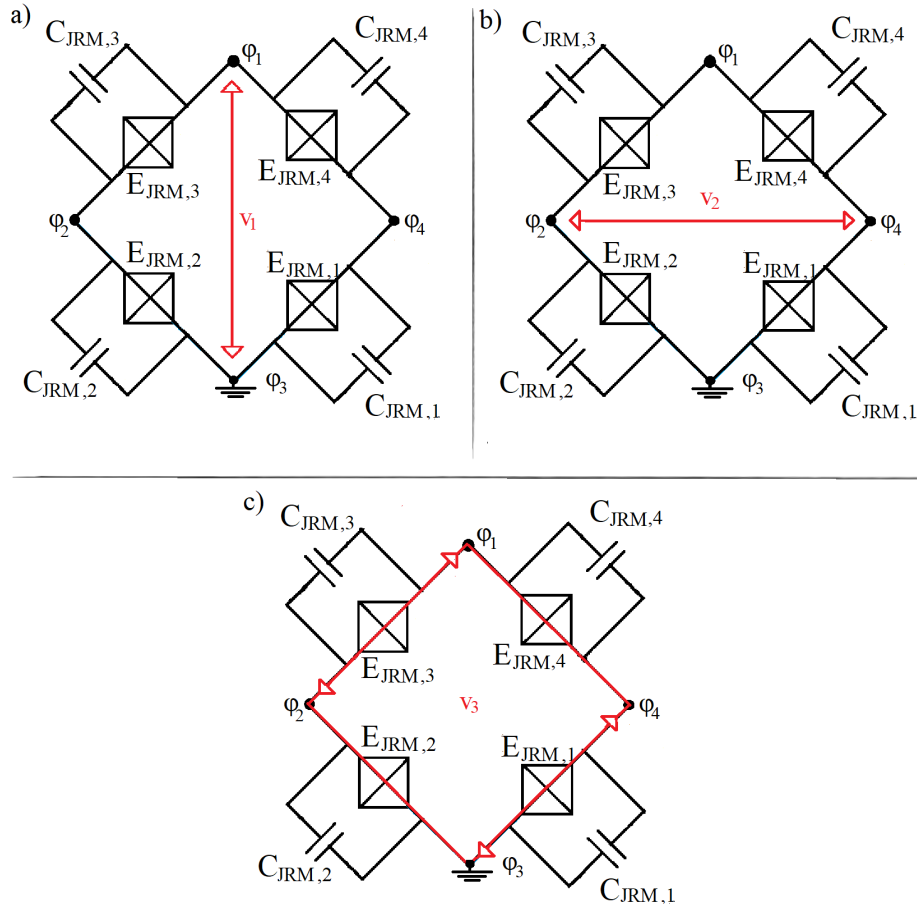


Figure 2.6: Illustration of a) eigenmode v_1 , b) eigenmode v_2 , and c) eigenmode v_3 of a JRM.

and the potential energy [14]

$$U(\Phi_m) = -E_J \cos(\sqrt{2}\Phi_{m,1}) - 4E_{JRM} \cos\left(\frac{\Phi_{m,1}}{\sqrt{2}}\right) \cos\left(\frac{\Phi_{m,2}}{\sqrt{2}}\right) \cos(\Phi_{m,3}).$$

In addition, one could introduce external magnetic flux Φ_{ext} flowing through the JRM ring. As a consequence, the Hamiltonian of JRM, expressed in terms of eigenmodes, is given by [21, 22]

$$\begin{aligned} \hat{\mathcal{H}}_{\text{ring}} = & -4E_J \cos\left(\frac{\Phi_{m,1}}{2\Phi_0}\right) \cos\left(\frac{\Phi_{m,2}}{2\Phi_0}\right) \cos\left(\frac{\Phi_{m,3}}{\Phi_0}\right) \cos\left(\frac{\Phi_{\text{ext}}}{4\Phi_0}\right) \\ & - 4E_J \sin\left(\frac{\Phi_{m,1}}{2\Phi_0}\right) \sin\left(\frac{\Phi_{m,2}}{2\Phi_0}\right) \sin\left(\frac{\Phi_{m,3}}{\Phi_0}\right) \sin\left(\frac{\Phi_{\text{ext}}}{4\Phi_0}\right), \end{aligned} \quad (2.22)$$

where $\Phi_{m,1} = \varphi_1 - \varphi_3$ labels the flux flowing between the node φ_1 and φ_3 , $\Phi_{m,2} = \varphi_2 - \varphi_4$ denotes the flux flowing between the node φ_2 and φ_4 , and $\Phi_{m,3} = \varphi_1 - \varphi_2 + \varphi_3 - \varphi_4$ represents the sum of flux $\varphi_1 - \varphi_2$ and flux $\varphi_3 - \varphi_4$.

2.4 Quantum Annealing

Quantum annealing is a protocol designed to solve hard optimization problems and is based on adiabatic quantum computation. The idea behind this protocol is to encode the solution of the optimization problem in the ground state of the Hamiltonian [5]

$$\hat{\mathcal{H}}_0 = - \sum_{i < j} J_{ij} \sigma_i^z \sigma_j^z - \sum_i h_i \sigma_i^z \quad (2.23)$$

where J_{ij} denotes the coupling strength between spins i and j , and h_i describes the magnetic field at site i . Then a suitably chosen non-commuting quantum tunneling Hamiltonian

$$\hat{\mathcal{H}}_1 = \sum_i \Delta_i \sigma_i^x \quad (2.24)$$

is to be added, where Δ_i denotes the interaction strength with the tunneling term. Hence, the total Hamiltonian takes the form

$$\hat{\mathcal{H}} = \hat{\mathcal{H}}_0 - \Gamma(t) \sum_i \Delta_i \sigma_i^x = \hat{\mathcal{H}}_0 + \hat{\mathcal{H}}_1(t), \quad (2.25)$$

where $\Gamma(t)$ denotes the time dependence of $\hat{\mathcal{H}}_1$ [5]. By numerically solving the time-dependent Schrödinger equation

$$i\hbar \frac{\partial |\Psi\rangle}{\partial t} = [\hat{\mathcal{H}}_0 + \hat{\mathcal{H}}_1(t)] |\Psi\rangle \quad (2.26)$$

starting with the ground state of the Hamiltonian, the final state of the Hamiltonian will be the ground state of $\hat{\mathcal{H}} = \hat{\mathcal{H}}_0$ for a sufficiently slow variation of $\Gamma(t)$ according to the adiabatic theorem [5]. Hereby, one designs the system such that $\Gamma(0) = 1$ and $\Gamma(\tau) = 0$, where τ is the annealing time.

2.5 Transmon Quantum Annealer

Here, the derivation of the circuit Hamiltonian on Fig. 1.1 is briefly presented. In order to derive the Lagrangian, the following fluxes $\Phi_{m,1} \equiv \Phi_1 - \Phi_3$, $\Phi_{m,2} \equiv \Phi_2 - \Phi_4$, and $\Phi_{m,3} \equiv \Phi_1 - \Phi_2 + \Phi_3 - \Phi_4$ are defined, where $\Phi_i = \int_{-\infty}^t V_i dt'$ is the flux variable defined as the time integral of the electrical potential V_i of island i [13]. The two differential modes $\Phi_{m,1}$ and $\Phi_{m,2}$ of the JRM are associated with the modes that couple the two flux signals Φ_a and Φ_b generated by two Transmon qubits by connecting them with conducting leads [13]. Under the assumption that all JRM junctions have the same Josephson energy E_{JRM} , all qubit capacitances C_J are equal, no parasitic capacitance is present, and no external magnetic

flux flows through the JRM loop, the Lagrangian is calculated as

$$L'_{2T} = \frac{C_J}{2} \dot{\Phi}_a^2 + E_{Ja} \cos\left(\frac{\Phi_a}{\Phi_0}\right) + \frac{C_J}{2} \dot{\Phi}_b^2 + E_{Jb} \cos\left(\frac{\Phi_b}{\Phi_0}\right) + 4E_{JRM} \cos\left(\frac{\Phi_a}{2\Phi_0}\right) \cos\left(\frac{\Phi_b}{2\Phi_0}\right) \cos\left(\frac{\Phi_z}{2\Phi_0}\right), \quad (2.27)$$

which after Legendre transformation and quantization becomes

$$\hat{\mathcal{H}}'_{2T} = 4E_C \hat{N}_a^2 - E_{Ja} \cos(\hat{\Phi}_a) + 4E_C \hat{N}_b^2 - E_{Jb} \cos(\hat{\Phi}_b) - 4E_{JRM} \cos\left(\frac{\hat{\Phi}_a}{2}\right) \cos\left(\frac{\hat{\Phi}_b}{2}\right) \quad (2.28)$$

for $\varphi_z = 0$. By introducing creation and annihilation operator

$$\hat{N}_x \equiv \frac{i}{2} \left(\frac{E_{Jx} + E_{JRM}}{2E_C} \right)^{1/4} (\hat{x} - \hat{x}^\dagger), \quad \hat{\Phi}_x \equiv \left(\frac{2E_C}{E_{Jx} + E_{JRM}} \right)^{1/4} (\hat{x} + \hat{x}^\dagger) \quad (2.29)$$

where $x \in \{a, b\}$. Truncating the Hamilton operator to the fourth order as well as performing a rotating wave approximation yields

$$\hat{\mathcal{H}}'_{2T} \approx \hat{\mathcal{H}}_{2T} = E_a \hat{a}^\dagger \hat{a} - \frac{E_C}{2} \hat{a}^\dagger \hat{a}^\dagger \hat{a} \hat{a} + E_b \hat{b}^\dagger \hat{b} - \frac{E_C}{2} \hat{b}^\dagger \hat{b}^\dagger \hat{b} \hat{b} - g(\hat{a} + \hat{a}^\dagger)^2 (\hat{b} + \hat{b}^\dagger)^2 \quad (2.30)$$

with

$$E_i \equiv \sqrt{8E_C(E_{Jx} + E_{JRM})} \quad (2.31)$$

$$g \equiv \frac{E_C}{2} \frac{E_{JRM}}{\sqrt{E_{Ja} + E_{JRM}} \sqrt{E_{Jb} + E_{JRM}}}.$$

Introducing microwave drives $\hat{\mathcal{H}}_{\text{drive}} = A_a(\hat{a}e^{i\omega_{d,a}t} + \hat{a}^\dagger e^{-i\omega_{d,a}t}) + A_b(\hat{b}e^{i\omega_{d,b}t} + \hat{b}^\dagger e^{-i\omega_{d,b}t})$ and transforming into a frame rotating with the microwave drives $\mathbf{U}_x = \exp(-i\omega_{d,x}tx^\dagger x)$ gives us the following Hamiltonian

$$\hat{\mathcal{H}}_{2T, \text{Qubit}} = A_a \sigma_x^a + A_b \sigma_x^b + J_a \sigma_z^a + J_b \sigma_z^b - g \sigma_z^a \sigma_z^b, \quad (2.32)$$

where $J_i \equiv E_i - 2\hbar g - \hbar\omega_{d,i}$ for $i \in \{a, b\}$ [13]. Hence, during annealing protocol, one needs to initially set up the microwave frequency equal to the corresponding $\frac{E_i}{\hbar} - 2g$ and continually reduces it to zero at $t \rightarrow \tau$, while the amplitude of the microwave starts at any small enough value and ends at zero.

In case of capacitors installed in parallel to each Josephson junction of JRM, the anharmonicity terms α_x are to be added to equation (2.30), which consequently modifies J_i in equation (2.32) to $J_i = E_i - \hbar\alpha_i - 2\hbar g - \hbar\omega_{d,i}$ [21].

Chapter 3

Results and Discussion

3.1 Deriving Circuit Hamiltonian

The first of all steps is to derive the Hamiltonian of our circuit, as depicted in 3.1, and examine several important information in it. As we incorporate a JRM to couple our Transmon qubits, our circuit consists of 4 nodes and 14 branches. These nodes comprise a ground node and 3 real nodes, therefore we expect 3 eigenmodes (X,Y, and Z) in accordance with the theoretical foundations described in Sec. 2.3. Meanwhile, of 14 branches, 3 are twigs, whereas the rests are links. Therefore, the dimension of f-cut matrix should be 3×14 , whilst the f-loop matrix should be of dimension 9×14 .

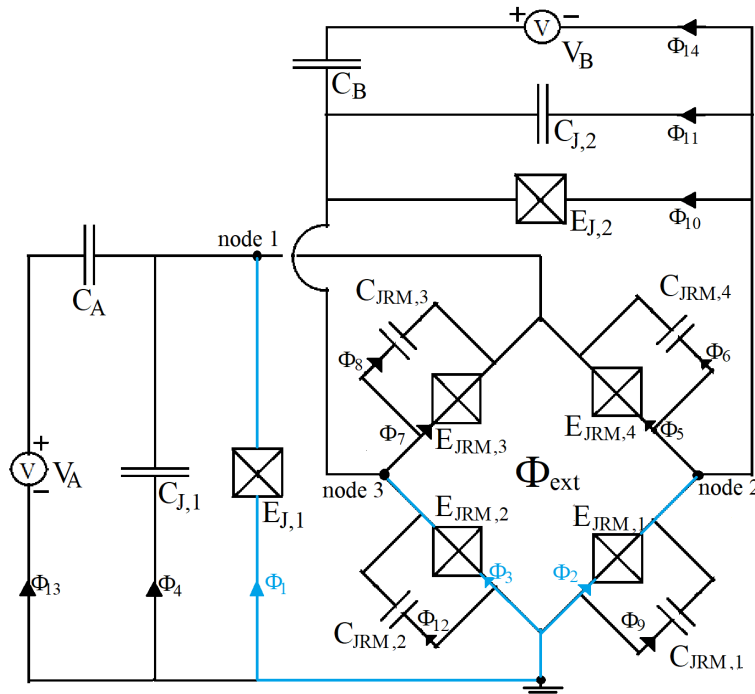


Figure 3.1: Circuit of two Transmon qubits coupled by a JRM. Each Transmon qubit is driven by its corresponding voltage source and an external magnetic flux flowing through the JRM loop is introduced. Here, the twigs are marked with blue lines.

Applying the electrical network graph theory from Sec. 2.1, the branches of our circuit are marked as $\Phi = (\Phi_t, \Phi_l)^T$, where $\Phi_t = (\Phi_1, \Phi_2, \Phi_3)^T$ are the twig branches and $\Phi_l = (\Phi_4, \dots, \Phi_{14})$ are the link branches. The f-cut as well as f-loop matrix are given by

$$\mathbf{F}^{(C)} = \begin{pmatrix} \mathbf{1} & \mathbf{F} \end{pmatrix}, \quad \mathbf{F}^{(L)} = \begin{pmatrix} -\mathbf{F}^T & \mathbf{1} \end{pmatrix},$$

$$\mathbf{F}^{(L)} = \begin{pmatrix} 1 & 1 & 1 & 1 & 1 & 0 & 0 & 0 & 0 & 1 & 0 \\ 0 & -1 & -1 & 0 & 0 & 1 & -1 & -1 & 0 & 0 & -1 \\ 0 & 0 & 0 & -1 & -1 & 0 & 1 & 1 & 1 & 0 & 1 \end{pmatrix}, \quad (3.1)$$

where the identity matrix $\mathbf{1}$ in $\mathbf{F}^{(C)}$ is of dimension 3×3 , whilst $\mathbf{1}$ in $\mathbf{F}^{(L)}$ has the dimension of 11×11 . One can then promptly determine the Lagrangian

$$\mathcal{L} = \frac{1}{2} (\dot{\Phi}_1 \dot{\Phi}_2 \dot{\Phi}_3) \mathbf{C} \begin{pmatrix} \dot{\Phi}_1 \\ \dot{\Phi}_2 \\ \dot{\Phi}_3 \end{pmatrix} + \mathbf{Q}_0 \cdot \begin{pmatrix} \dot{\Phi}_1 \\ \dot{\Phi}_2 \\ \dot{\Phi}_3 \end{pmatrix} - \frac{1}{2} (\Phi_1 \Phi_2 \Phi_3) \mathbf{L}^{-1} \begin{pmatrix} \Phi_1 \\ \Phi_2 \\ \Phi_3 \end{pmatrix}$$

$$- \left(\mathbf{S} \cdot \Phi_{\text{ext}} \begin{pmatrix} \Phi_1 \\ \Phi_2 \\ \Phi_3 \end{pmatrix} + C \cdot \Phi_{\text{ext}}^2 \right) + \mathcal{L}_{\text{nl}} \quad (3.2)$$

with

$$\mathbf{C} = \begin{pmatrix} C_A + C_{J1} + C_{JRM3} + C_{JRM4} & -C_{JRM4} & -C_{JRM3} \\ -C_{JRM4} & C_B + C_{J2} + C_{JRM1} + C_{JRM4} & -C_B - C_{J2} \\ -C_{JRM3} & -C_B - C_{J2} & C_B + C_{J2} + C_{JRM2} + C_{JRM3} \end{pmatrix},$$

$$\mathbf{L}^{-1} = \begin{pmatrix} E_{J1} + E_{JRM3} + E_{JRM4} & -E_{JRM4} & -E_{JRM3} \\ -E_{JRM4} & E_{J2} + E_{JRM1} + E_{JRM4} & -E_{J2} \\ -E_{JRM3} & -E_{J2} & E_{J2} + E_{JRM2} + E_{JRM3} \end{pmatrix} \cdot \frac{1}{\Phi_0^2}, \quad (3.3)$$

$$\mathbf{Q}_0 = \begin{pmatrix} C_{JRM4} \dot{\Phi}_{\text{ext}} - C_A V_A \\ -C_{J2} \dot{\Phi}_{\text{ext}} - C_{JRM4} \dot{\Phi}_{\text{ext}} - C_B (\dot{\Phi}_{\text{ext}} - V_B) \\ C_{J2} \dot{\Phi}_{\text{ext}} + C_B (\dot{\Phi}_{\text{ext}} - V_B) \end{pmatrix},$$

$$\mathbf{S} = \begin{pmatrix} E_{JRM4} \\ -E_{JRM4} - E_{J2} \\ E_{J2} \end{pmatrix} \cdot \frac{1}{\Phi_0^2}, \quad C = \frac{E_{JRM4} + E_{J2}}{2\Phi_0^2},$$

and the non-linear Lagrangian as well as its approximation

$$\begin{aligned}
 \mathcal{L}_{\text{nl}} &= E_{\text{J1}} \left(\cos\left(\frac{\Phi_1}{\Phi_0}\right) + \frac{\Phi_1^2}{2\Phi_0^2} - 1 \right) + E_{\text{JRM1}} \left(\cos\left(\frac{\Phi_2}{\Phi_0}\right) + \frac{\Phi_2^2}{2\Phi_0^2} - 1 \right) \\
 &+ E_{\text{JRM2}} \left(\cos\left(\frac{\Phi_3}{\Phi_0}\right) + \frac{\Phi_3^2}{2\Phi_0^2} - 1 \right) + E_{\text{JRM3}} \left(\cos\left(\frac{\Phi_1 - \Phi_3}{\Phi_0}\right) + \frac{(\Phi_1 - \Phi_3)^2}{2\Phi_0^2} - 1 \right) \\
 &+ E_{\text{JRM4}} \left(\cos\left(\frac{\Phi_1 - \Phi_2 + \Phi_{\text{ext}}}{\Phi_0}\right) + \frac{(\Phi_1 - \Phi_2 + \Phi_{\text{ext}})^2}{2\Phi_0^2} - 1 \right) \\
 &+ E_{\text{J2}} \left(\cos\left(\frac{-\Phi_2 + \Phi_3 + \Phi_{\text{ext}}}{\Phi_0}\right) + \frac{(-\Phi_2 + \Phi_3 + \Phi_{\text{ext}})^2}{2\Phi_0^2} - 1 \right), \tag{3.4}
 \end{aligned}$$

$$\begin{aligned}
 \mathcal{L}_{\text{nl}} \approx & E_{\text{J1}} \frac{\Phi_1^4}{4!\Phi_0^4} + E_{\text{JRM1}} \frac{\Phi_2^4}{4!\Phi_0^4} + E_{\text{JRM3}} \frac{(\Phi_1 - \Phi_3)^4}{4!\Phi_0^4} + E_{\text{JRM2}} \frac{\Phi_3^4}{4!\Phi_0^4} + E_{\text{JRM4}} \frac{(\Phi_1 - \Phi_2 + \Phi_{\text{ext}})^4}{4!\Phi_0^4} \\
 &+ E_{\text{J2}} \frac{(-\Phi_2 + \Phi_3 + \Phi_{\text{ext}})^4}{4!\Phi_0^4}.
 \end{aligned}$$

Here, the truncation to fourth order is only applied for the case without driving. Later, when the qubits are driven, we abstain from the truncation and treat the non-linear Lagrangian as such.

The linear part of the Lagrangian in Eq. (3.2), which comprises the capacitive term \mathbf{C} and the inductive term \mathbf{L}^{-1} , can easily be diagonalized by diagonalizing the capacitive part and then the inductive part, following the recipe from Subsec. 2.1.3, yielding the following Lagrangian

$$\tilde{\mathcal{L}} = \frac{1}{2} \dot{\Phi}_m^T \Lambda \check{\mathbf{C}} \mathbf{I}_{\mathbf{C}} \dot{\Phi}_m - \frac{1}{2} \Phi_m^T \mathbf{I}_{\mathbf{L}}^{-1} \Phi_m + \mathbf{Q}_0 \cdot (\mathbf{E} \dot{\Phi}_m) - \left(\mathbf{S} \cdot \mathbf{E} \Phi_{\text{ext}} \Phi_m + C \Phi_{\text{ext}}^2 \right) + \tilde{\mathcal{L}}_{\text{nl}}(\Phi_t(\Phi_m)), \tag{3.5}$$

where $\mathbf{E} \equiv \mathbf{O}_{\mathbf{L}} \Lambda_{\mathbf{L}}^{1/2} \mathbf{O}_{\mathbf{C}}$ is the basis change matrix, which expresses Φ_t in terms of eigenmodes Φ_m . A Legendre transformation is then performed on Eq. (3.5), providing the Hamiltonian

$$\mathcal{H} = \frac{1}{2} \mathbf{Q}_m^T \Omega^2 \mathbf{I}_{\mathbf{L}} \mathbf{Q}_m + \frac{1}{2} \Phi_m^T \mathbf{I}_{\mathbf{L}}^{-1} \Phi_m - \mathbf{Q}_0 \cdot \mathbf{E} \Omega^2 \mathbf{I}_{\mathbf{L}} \mathbf{Q}_m + \left(\mathbf{S} \cdot \mathbf{E} \Phi_{\text{ext}} \Phi_m + C \Phi_{\text{ext}}^2 \right) - \tilde{\mathcal{L}}_{\text{nl}}(\Phi_t(\Phi_m)). \tag{3.6}$$

Now, we examine the Hamiltonian from Eq. (3.6) without driving. This eliminates the offset charges \mathbf{Q}_0 and the external magnetic flux Φ_{ext} , leaving only the first, second, and last term of Eq. (3.6). By introducing creation and annihilation operator for quantization as given by Eq. (2.16), one obtains the

quantized Hamiltonian after algebraic simplification

$$\begin{aligned}
 \hat{\mathcal{H}} = & \sum_{k=1}^3 \hbar\omega_k (\hat{a}_k^\dagger \hat{a}_k + 1/2) - \sum_{k=1}^3 \frac{\hbar\alpha_k}{12} (\hat{a}_k^\dagger + \hat{a}_k)^4 - \sum_k \sum_{j \neq k} \frac{\hbar g_{jk}^z}{4} (\hat{a}_j^\dagger + \hat{a}_j)^2 (\hat{a}_k^\dagger + \hat{a}_k)^2 \\
 & + \sum_{k=1}^3 \sum_{j \neq k} \sum_{i \neq j, i \neq k} \hbar \xi_k (\hat{a}_k^\dagger + \hat{a}_k)^2 (\hat{a}_j^\dagger + \hat{a}_j) (\hat{a}_i^\dagger + \hat{a}_i) \\
 & + \sum_k \sum_{j \neq k} \hbar g_{jk}^{x,1} (\hat{a}_k^\dagger + \hat{a}_k)^3 (\hat{a}_j^\dagger + \hat{a}_j) + \hbar g_{jk}^{x,2} (\hat{a}_k^\dagger + \hat{a}_k) (\hat{a}_k^\dagger + \hat{a}_k)^3,
 \end{aligned} \tag{3.7}$$

where ω_k , α_k , and g_{jk}^z is the eigenfrequency of eigenmode k , the anharmonicity of eigenmode k , and the coupling between qubit k and j , respectively. In this work, we mainly work with the following parameter values: $\forall i \in \{1,2,3,4\} E_{\text{JRM},i}/\hbar = E_{\text{JRM}}/\hbar = 13$ GHz, $C_{\text{JRM},i} = C_{\text{JRM}} = 100$ fF, $E_{\text{J1}}/\hbar = E_{\text{J2}}/\hbar = 11$ GHz, and $C_{\text{J1}} = C_{\text{J2}} = 50$ fF. Using these parameters, we recognize that $\xi_k, g_{jk}^{x,1}, g_{jk}^{x,2} \approx \mathcal{O}(10^{-7} \text{ rad } s^{-1})$, while $\omega_k, \alpha_k, g_{jk}^z \gg \mathcal{O}(10^{-7} \text{ rad } s^{-1})$. For this reason, the last two terms of Eq. (3.7) can be safely ignored. Numerical calculation involving Mathematica yields the following parameter values

$$\begin{aligned}
 \omega_1 &\approx 2\pi \cdot 4.98 \cdot 10^9 \text{ Hz}, & \omega_2 &\approx 2\pi \cdot 4.98 \cdot 10^9 \text{ Hz}, & \omega_3 &\approx 2\pi \cdot 4.49 \cdot 10^9 \text{ Hz}, \\
 \alpha_1 &\approx 2\pi \cdot 76.67 \cdot 10^6 \text{ Hz}, & \alpha_2 &\approx 2\pi \cdot 76.67 \cdot 10^6 \text{ Hz}, & \alpha_3 &\approx 2\pi \cdot 48.43 \cdot 10^6 \text{ Hz}, \\
 g_{12}^z &\approx 2\pi \cdot 34.96 \cdot 10^6 \text{ Hz}, & g_{13}^z &\approx 2\pi \cdot 58.20 \cdot 10^6 \text{ Hz}, & g_{23}^z &\approx 2\pi \cdot 58.20 \cdot 10^6 \text{ Hz}.
 \end{aligned} \tag{3.8}$$

One notices here that $\omega_1 = \omega_2$ due to the symmetry of our parameters choice for the JRM. These eigenfrequencies correspond to the X and Y eigenmode, whose corresponding qubits are driven later with voltage source and external magnetic flux, whereas the last ω_3 is associated with Z eigenmode, whose corresponding qubit is only driven by external magnetic flux. The numerically obtained value of $\omega_1, \omega_2, \omega_3$, and α_3 confirm the work of Leib [13] and Roy [21], where the analytical expressions for these variables are derived [13, 21] and the existence of third qubit arising from parasitic capacitance is presented. These analytical expressions are

$$\begin{aligned}
 \omega_1 &= \frac{\sqrt{8(E_{\text{JRM}} + E_{\text{J1}})E_{C_{\text{J1}}}}}{\hbar}, & \omega_2 &= \frac{\sqrt{8(E_{\text{JRM}} + E_{\text{J2}})E_{C_{\text{J2}}}}}{\hbar}, \\
 \omega_3 &= \frac{\sqrt{32E_{\text{JRM}}E_{C_{\text{JRM}}}}}{\hbar}, & \alpha_3 &= \frac{E_{C_{\text{JRM}}}}{\hbar},
 \end{aligned} \tag{3.9}$$

where

$$E_{C_{\text{J1}}} = \frac{e^2}{2(C_{\text{J1}} + C_{\text{JRM}})}, \quad E_{C_{\text{J2}}} = \frac{e^2}{2(C_{\text{J2}} + C_{\text{JRM}})}, \quad E_{C_{\text{JRM}}} = \frac{e^2}{8C_{\text{JRM}}}. \tag{3.10}$$

In order to have an insight to the eigenmodes of our circuit, the inverse of \mathbf{E} is simply determined,

thereby expressing Φ_m in terms of twigs basis Φ_i . By this mean, we obtain

$$\tilde{\mathbf{v}}_1 \approx (-1, 0, 0)^T, \quad \tilde{\mathbf{v}}_2 \approx \left(0, \frac{-1}{\sqrt{2}}, \frac{1}{\sqrt{2}}\right)^T, \quad \tilde{\mathbf{v}}_3 \approx \left(\frac{1}{\sqrt{3}}, \frac{-1}{\sqrt{3}}, \frac{-1}{\sqrt{3}}\right)^T.$$

Through comparison with the eigenmodes reported by Rasmussen [14] and Roy [21] as written in Sec. 2.3, we recognize that $\tilde{\mathbf{v}}_i$ corresponds with \mathbf{v}_i for $i \in \{1,2,3\}$ in Sec. 2.3. The difference here is that $\tilde{\mathbf{v}}_{\text{CM}}$ is not revealed in our result, as we set one node as ground node. In addition, we express our eigenmodes as flux flowing between nodes, whereas in Sec. 2.3 the eigenmodes are presented in terms of flux flowing to or from nodes. Moreover, one notices here that $\tilde{\mathbf{v}}_1$ is perpendicular to $\tilde{\mathbf{v}}_2$, which is in turn orthogonal to $\tilde{\mathbf{v}}_3$. The eigenmode $\tilde{\mathbf{v}}_1$ ($\tilde{\mathbf{v}}_2$) corresponds to Y-eigenmode (X-eigenmode) and the eigenmode $\tilde{\mathbf{v}}_3$ corresponds to Z-eigenmode. For the annealing protocol, the qubit associated with Y (X) mode is driven with the voltage source V_A (V_B), which is installed in parallel with Φ_1 (Φ_{10}) and Φ_4 -branches (Φ_{11} -branches), whilst the third qubit from Z-eigenmode $\tilde{\mathbf{v}}_3$ is not driven by voltage source. The coupling g between these 3 qubits is controlled via external magnetic flux Φ_{ext} , which drives all qubits and is deactivated slowly during annealing protocol.

For clarity, the visualization of each eigenmode in terms of flowing fluxes is illustrated in Fig. 3.2.

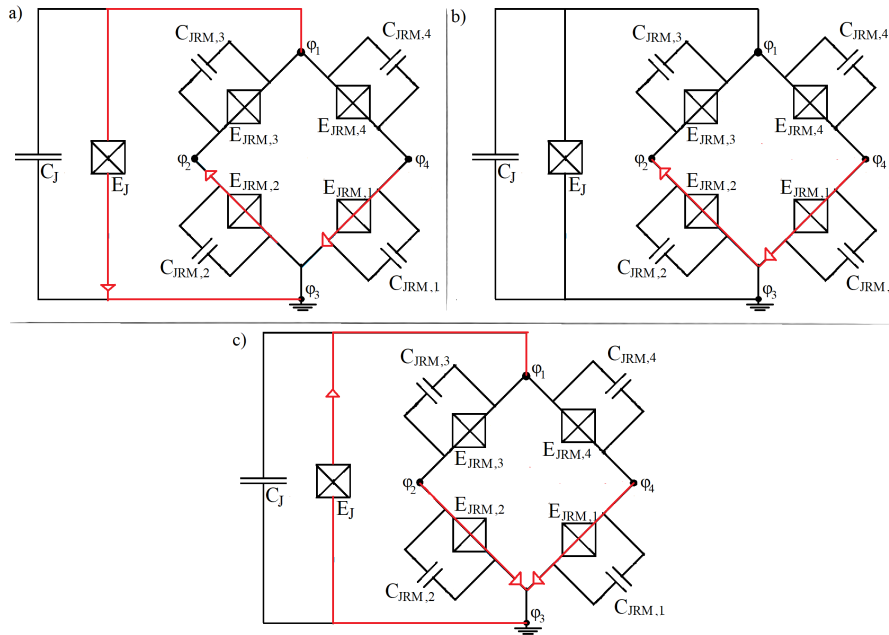


Figure 3.2: Illustration of a) eigenmode $\tilde{\mathbf{v}}_1$, b) eigenmode $\tilde{\mathbf{v}}_2$, and c) eigenmode $\tilde{\mathbf{v}}_3$ of JRM with a transmon qubit. The red arrows depict the flow direction of the twig fluxes for their corresponding eigenmodes. This figure depicts a part of full circuit in Fig. 3.1

3.2 Quantum Annealing

For the rest of Sec. 3.2, we work with the circuit illustrated in Fig. 3.1. This circuit has the Hamiltonian

$$\hat{\mathcal{H}} = \frac{1}{2} \hat{\mathbf{Q}}_m^T \boldsymbol{\Omega}^2 \mathbf{I}_L \hat{\mathbf{Q}}_m + \frac{1}{2} \hat{\boldsymbol{\Phi}}_m^T \mathbf{I}_L^{-1} \hat{\boldsymbol{\Phi}}_m - \mathbf{Q}_0 \cdot \mathbf{E} \boldsymbol{\Omega}^2 \mathbf{I}_L \hat{\mathbf{Q}}_m + \left(\mathbf{S} \cdot \mathbf{E} \Phi_{\text{ext}} \hat{\boldsymbol{\Phi}}_m + C \Phi_{\text{ext}}^2 \right) - \tilde{\mathcal{L}}_{\text{nl}}(\hat{\boldsymbol{\Phi}}_t(\hat{\boldsymbol{\Phi}}_m)), \quad (3.11)$$

which results from the quantization of Eq. (3.6), following the recipe from Eq. (2.16).

For the purpose of annealing process, the frequency of the microwave drive ω_A (ω_B) is set initially equal to ω_1 (ω_2) from Eq. (3.8). This frequency is linearly reduced, until it vanishes at $t \rightarrow \tau$. At the same time, the amplitude of our voltage source is also diminished, following the relation $V_{A,B} \sim (1 - \sqrt[20]{t/\tau})$. This dependency is chosen, in order to suppress the voltage amplitude quickly at the beginning. As we shall see, the voltage amplitude turns out to be proportional to the eigenenergy fluctuation over time, for which reason the observation of eigenenergy evolution would be hampered, if the amplitude is too large. Furthermore, the applied external magnetic flux begins at $\Phi_{\text{ext}} = 2\pi\Phi_0$ and is linearly decreased to zero at $t = \tau$.

In summary, the protocol of our quantum annealing is given by

$$\begin{aligned} V_A(t) &= V_0 \left(1 - \sqrt[20]{\frac{t}{\tau}} \right) \cos(\omega_A t), & \omega_A(t) &= \omega_Y \left(1 - \frac{t}{\tau} \right), \\ V_B(t) &= V_0 \left(1 - \sqrt[20]{\frac{t}{\tau}} \right) \cos(\omega_B t), & \omega_B(t) &= \omega_X \left(1 - \frac{t}{\tau} \right), \\ \Phi_{\text{ext}}(t) &= \Phi_{\text{ext},0} \left(1 - \frac{t}{\tau} \right), & \Phi_{\text{ext},0} &= 2\pi\Phi_0, \end{aligned} \quad (3.12)$$

where V_0 is the initial voltage amplitude, τ is the annealing time, and Φ_0 is the reduced magnetic flux quantum.

3.2.1 Idealized Quantum Annealing

Our next goal is to understand the behavior of the evolving eigenstate during the annealing protocol. To proceed, we ignore the interaction with the environment and first simulate the time evolution of eigenenergies under idealized circumstances with QuTip [23, 24]. For this, we set $\tau = 1 \mu\text{s}$. The choice of annealing time τ is arbitrary, as our program only numerically solves the eigenvalue problem of the circuit Hamiltonian. Not only that we are interested in the influence of initial voltage amplitude V_0 during the course of eigenenergy evolution, but also the study of this time evolution is necessary to extract minimum energy gap ΔE_{min} between the ground energy E_0 and the first excited energy E_1 . Information about the minimum energy gap enables us to estimate the time, which the annealing time

τ needs to significantly exceed, such that the state evolves adiabatically, as given by [25]

$$\tau \gg \gg O\left(\frac{1}{\Delta E_{\min}^2}\right). \quad (3.13)$$

The evolution of three lowest eigenenergies as well as the energy difference to the ground energy are depicted in Fig. 3.3. The first feature one can recognize is that the main course of eigenenergies is approximately symmetrical with respect to red dashed vertical line. We attribute this result to the even property of the cosine, which appears as $\cos\left(\frac{\Phi_1 - \Phi_2 + \Phi_{\text{ext}}}{\Phi_0}\right)$ and $\cos\left(\frac{-\Phi_2 + \Phi_3 + \Phi_{\text{ext}}}{\Phi_0}\right)$ in $\tilde{\mathcal{L}}_{\text{nl}}(\hat{\Phi}_t(\hat{\Phi}_m))$ (see Eq. (3.4) or Eq. (3.11)), and the small flux $\hat{\Phi}_i$ for $i \in \{1,2,3\}$ according to transmon's resilience to the ubiquitous charge noise during whole annealing process [13]. Due to this reason, every term in $\tilde{\mathcal{L}}_{\text{nl}}(\hat{\Phi}_t(\hat{\Phi}_m))$ except those containing Φ_{ext} -dependency can be approximated as vanishingly small and Φ_{ext} becomes the main contributor of $\cos\left(\frac{\Phi_1 - \Phi_2 + \Phi_{\text{ext}}}{\Phi_0}\right)$ and $\cos\left(\frac{-\Phi_2 + \Phi_3 + \Phi_{\text{ext}}}{\Phi_0}\right)$. Meanwhile, the quadratic terms are eliminated by terms from \mathbf{L}^{-1} , \mathbf{S} , and \mathbf{C} , as these terms emerge only due to the expansion of \mathcal{L}_{nl} in Eq. (3.4) prior to quantization. As a consequence, the term $\cos\left(\frac{\Phi_1 - \Phi_2 + \Phi_{\text{ext}}}{\Phi_0}\right)$ and $\cos\left(\frac{-\Phi_2 + \Phi_3 + \Phi_{\text{ext}}}{\Phi_0}\right)$ exhibits vertical symmetry with respect to $t \approx 0.5\tau$, at which $\Phi_{\text{ext}} = \pi\Phi_0$. The second observation is that the initial voltage amplitude positively influences the oscillation of eigenenergy, particularly in the beginning of annealing process, as Fig. 3.3(e) and 3.3(f) exhibit stronger oscillations than Fig. 3.3(a) and Fig. 3.3(b). We think that this occurs since the increase of initial voltage amplitude would influence the potential landscape of our circuit's Hamiltonian more strongly and thus causes stronger eigenenergy oscillation. As strong eigenenergy oscillation hinders the observation of the main eigenenergy evolution, the voltage amplitude is chosen to be $V_{\text{A,B}} \sim (1 - \sqrt[20]{t/\tau})$ as described in Sec. 3.2. Another remarkable observation is that the energy gap between the first (second) excited state and the ground state $\Delta E_{\min,10}/h$ ($\Delta E_{\min,20}/h$) occurs around $t/\tau \approx 0.5$. Around this point, $\Delta E_{\min,10}/h$ ($\Delta E_{\min,20}/h$) amounts to approximately 164.65 MHz (3.64 GHz), 164.91 MHz (3.64 GHz), and 187.09 MHz (3.62 GHz) for $V_0 = 1.26 \mu\text{V}$, $V_0 = 150 \mu\text{V}$, and $V_0 = 1.8 \text{ mV}$, respectively. Apparently, the initial voltage amplitude does not have substantial effect on the minimum energy gap.

The second step of studying how the eigenstate behaves during the annealing process is to investigate the effect of annealing time τ on the fidelity $\mathcal{F}^2(t) \equiv |\langle \phi_0(t) | \psi(t) \rangle|^2$, which is a measure of how close the evolving eigenstate $|\psi(t)\rangle$ is to instantaneous ground state $|\phi_0(t)\rangle$ of the Hamiltonian. In the best case, by which $\tau \rightarrow \infty$, we would have perfectly adiabatic process such that $\mathcal{F}^2 \rightarrow 1$. In the other extreme case, where $\tau \rightarrow 0$, we would have a perfectly diabatic process and \mathcal{F}^2 would move away from 1, because the eigenstate cannot adapt to the changing Hamiltonian and might be excited to the next higher states.

In order to attain the changing eigenstate $|\psi(t)\rangle$ in dependence of time, we numerically solve the Schrödinger equation and eigenvalue problem

$$i\hbar \frac{\partial |\psi(t)\rangle}{\partial t} = \hat{\mathcal{H}}(t) |\psi(t)\rangle, \quad \hat{\mathcal{H}}(t) |\phi_0(t)\rangle = E_0 |\phi_0(t)\rangle, \quad (3.14)$$

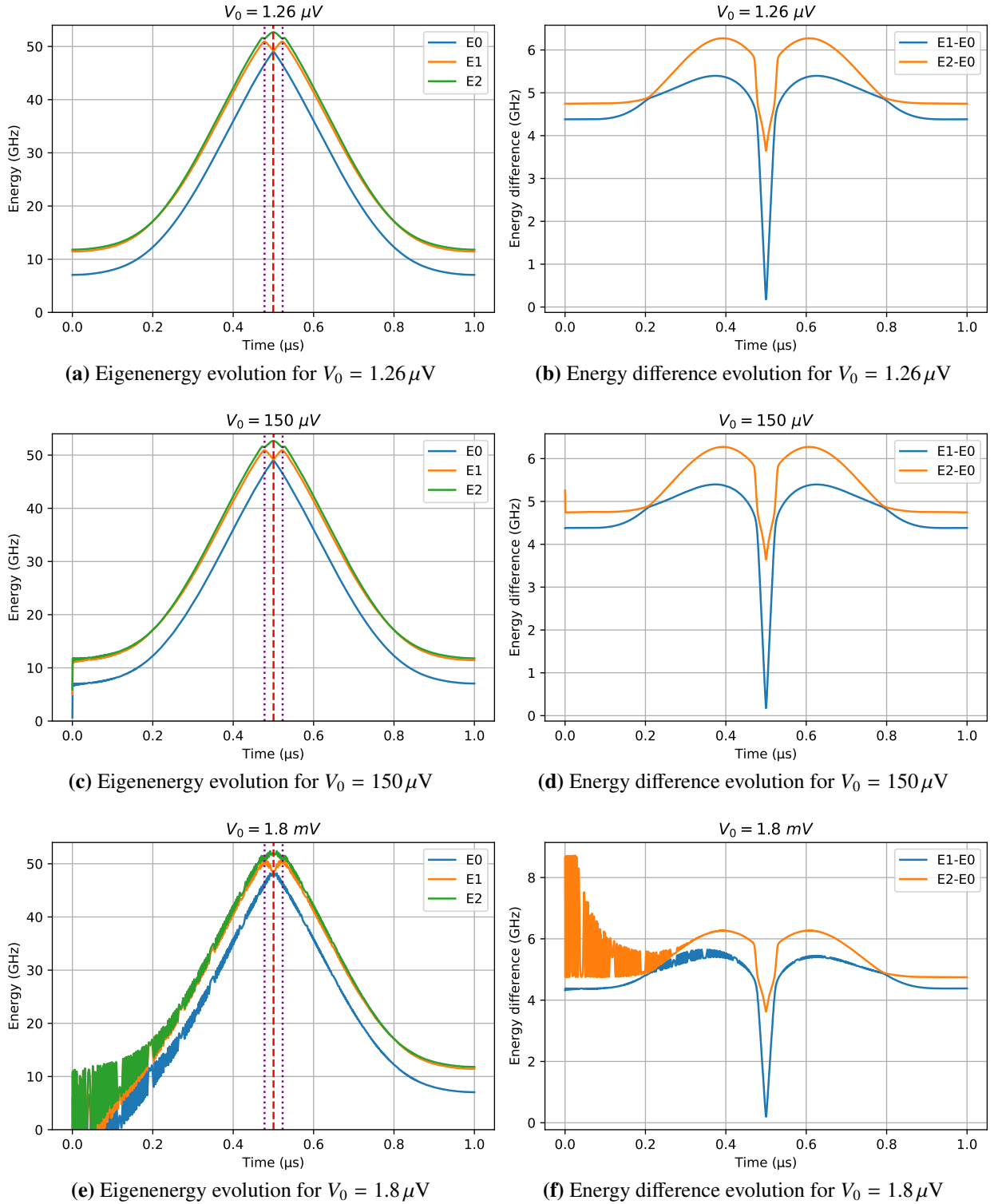


Figure 3.3: Selected eigenenergies and eigenenergy differences as a function of time. The time, when the minimal gap $\Delta E_{\min,10}$ and $\Delta E_{\min,20}$ are reached, is marked with the red dashed line, while the local minimal gap $\Delta E_{\min,21}$ is marked with the purple dotted line. The following parameter values: $\forall i \in \{1,2,3,4\} E_{\text{JRM},i}/h = E_{\text{JRM}}/h = 13 \text{ GHz}$, $C_{\text{JRM},i} = C_{\text{JRM}} = 100 \text{ fF}$, $E_{\text{J1}}/h = E_{\text{J2}}/h = 11 \text{ GHz}$, and $C_{\text{J1}} = C_{\text{J2}} = 50 \text{ fF}$ are used

using QuTip during annealing process, where the initial state of $|\psi(0)\rangle$ is the ground state of the initial Hamiltonian $\hat{\mathcal{H}}(0)$. By this mean, we are able to calculate the fidelity or infidelity and thus determines the final fidelity $\mathcal{F}^2(\tau)$ or final infidelity $1 - \mathcal{F}^2(\tau)$. Hereafter, we can plot the final infidelity in dependence of the annealing time, which is illustrated in Fig. 3.4.

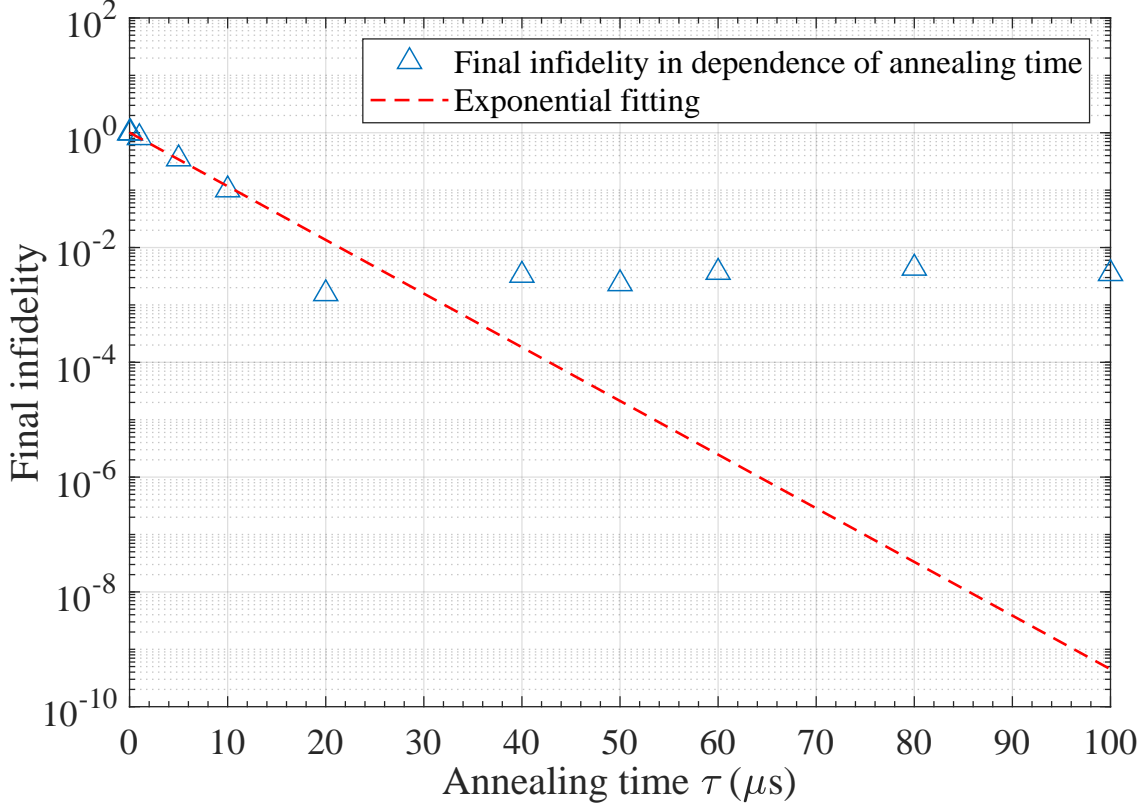


Figure 3.4: Final infidelity $1 - \mathcal{F}^2(\tau)$ in dependence of annealing time τ (μs). The following parameter values: $\forall i \in \{1,2,3,4\} E_{\text{JRM},i}/\hbar = E_{\text{JRM}}/\hbar = 13$ GHz, $C_{\text{JRM},i} = C_{\text{JRM}} = 100$ fF, $E_{\text{J1}}/\hbar = E_{\text{J2}}/\hbar = 11$ GHz, $C_{\text{J1}} = C_{\text{J2}} = 50$ fF, and $V_0 = 1.26$ μV are used.

One can qualitatively recognize in Fig. 3.4 that the final infidelity is inversely proportional to the annealing time τ , obeying the adiabatic theorem. However, our simulation shows that the final infidelity starts to get saturated around $\tau \approx 20$ μs and deviates from our exponential fit function for $\tau > 20$ μs . This exponential fit is an attempt to attain a phenomenological description of final infidelity behavior and is numerically determined using Matlab, which yields the following value

$$1 - \mathcal{F}^2(\tau) = a \cdot e^{-b\tau}, \quad a = 1.006 \pm 0.0138, \quad b = (0.2153 \pm 0.0104) \text{ MHz},$$

where τ is in μs . The exponential function is intentionally chosen as fit function, in order to mimic the Landau-Zener formula of diabatic transition probability [26]

$$P_{\text{na}} = \exp\left\{-2\pi \frac{|H_{12}|}{\hbar} \frac{|H_{12}|}{v|F_{12}|}\right\}, \quad (3.15)$$

where H_{12} is the constant coupling matrix element in the diabatic basis, $F_{12} \equiv F_1 - F_2$ is the difference between the slope 1 of $E_1(x)$ and slope 2 of $E_2(x)$, and v is the magnitude of the relative velocity $\dot{x}(t)$, which is assumed constant throughout. The fact that our circuit Hamiltonian does not have constant H_{12} , F_{12} , and v may cause the deviation of final infidelity for $\tau > 20 \mu\text{s}$ from the exponential fit.

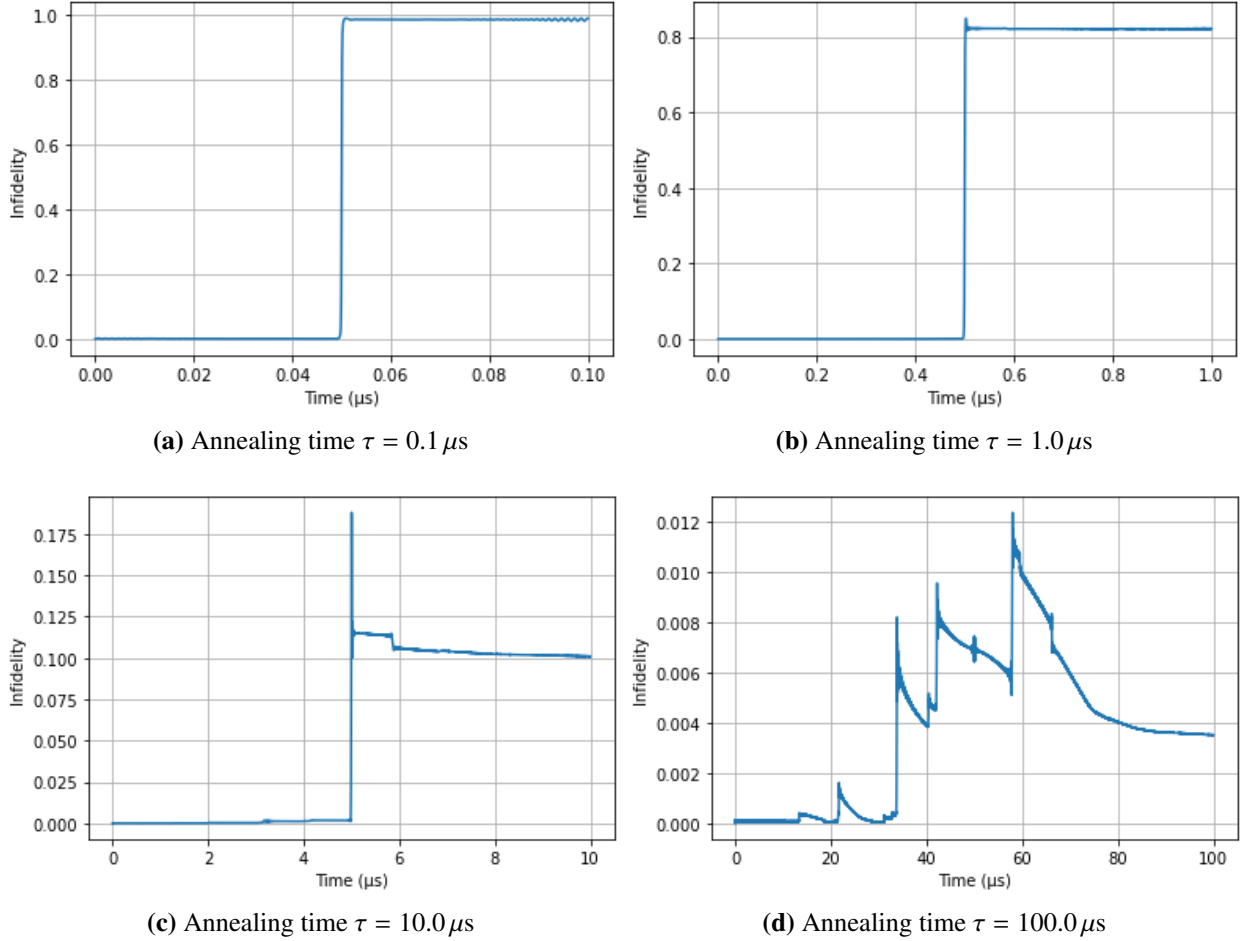


Figure 3.5: Infidelity $1 - \mathcal{F}^2(t)$ as a function of time. The following parameter values: $\forall i \in \{1,2,3,4\} E_{\text{JRM},i}/h = E_{\text{JRM}}/h = 13 \text{ GHz}$, $C_{\text{JRM},i} = C_{\text{JRM}} = 100 \text{ fF}$, $E_{\text{J1}}/h = E_{\text{J2}}/h = 11 \text{ GHz}$, $C_{\text{J1}} = C_{\text{J2}} = 50 \text{ fF}$, and $V_0 = 1.26 \mu\text{V}$ are used.

In addition, we are also interested in the change of the eigenstate during the annealing process, in particular for low τ , for which the state is not close to the instantaneous ground state of the corresponding Hamiltonian $\hat{\mathcal{H}}(t)$. Therefore, we show Fig. 3.5, which depicts the course of infidelity in dependence of time for four various annealing times.

One can easily notice that, except for Fig. 3.5(d), a rapid growth of the infidelity occurs around $t/\tau \approx 0.5$, where the Hamiltonian of our circuit has the minimum energy gap $\Delta E_{\text{min},10}$, as marked with red dashed line in Fig. 3.3. We suspect that due to quick annealing process, the eigenstate does not have suffice time to evolve into the instantaneous Hamiltonian's ground state at $t/\tau \approx 0.5 \mu\text{s}$ and thus

has higher probability to be excited to the higher states. This statement is, however, only a hypothesis. Hence, the exact reason, why the infidelity rapidly jumps at the minimum energy gap $\Delta E_{\min,10}$, needs to be investigated further. This investigation is unfortunately not carried out due to the limited time frame of this work.

Because we deal with an adiabatic process, we naturally want to understand the change of the eigenstate during the annealing process, especially around the time, at which the infidelity climbs rapidly. Therefore, using QuTip we track the path of state evolution through calculation of the probability for excitation in the higher states. For this calculation, the instantaneous ground state $\langle \phi_0(t) |$ in the definition of the fidelity $\mathcal{F}^2(t)$ is substituted with instantaneous higher states, i.e. first (second) excited state $\langle \phi_1(t) |$ ($\langle \phi_2(t) |$). The corresponding results are shown in Fig. 3.6, which exhibits the probability of transition to the first and second excited state. We are aware that transitions to even higher states are also possible. Hence, the cumulative probability to find the system in either one of three lowest states is also determined via $P_{\text{cum}}(t) = \mathcal{F}^2(t) + |\langle \phi_1(t) | \psi(t) \rangle|^2 + |\langle \phi_2(t) | \psi(t) \rangle|^2$, which is displayed in Fig. 3.7. One could easily observe the trend in Fig. 3.6 that the probability of transitions to higher states decreases with increasing annealing time τ . Likewise, the cumulative probability in Fig. 3.7 tends to be closer to the value 1 with increasing annealing time. This can be attributed again to the behavior of evolving state, which more closely resembles an adiabatic process for longer annealing times, as the Hamiltonian is changed more slowly. For the particularly short annealing times like $\tau = 0.01 \mu\text{s}$ and $\tau = 0.1 \mu\text{s}$, the probability of excitation to first or second excited state is relatively small at the beginning until it bypasses the first $\Delta E_{\min,21}$ marked by left purple dotted line. Around this time point, the state still behaves adiabatically as it is still in ground state and the point $\Delta E_{\min,10}$ or $\Delta E_{\min,20}$ has not been reached. However, as the state evolution reaches the point, where the minimum gap $\Delta E_{\min,10}$ occurs, the state can no longer adapt to the instantaneous ground state and could thus be excited to the first state E_1 with certain probability. Yet, the transition to second state E_2 around this point is still improbable, because $\Delta E_{\min,20}$ is still too large. When the state reaches the second $\Delta E_{\min,21}$ labeled with the right purple dotted line, it can, however, be excited to the second state, since it is now in the first excited state and hence requires less energy for transition to the next higher state. After the state passes this time point, the probability of transition to both E_1 and E_2 for annealing time $\tau = 0.01 \mu\text{s}$ drops in sudden. This sudden decrease is, however, not attributed to the transition to ground state, but rather the excitation to next higher states, since Fig. 3.7(a) likewise displays a rapid decline, indicating low probability of the system in either one of three lowest eigenstates. The similar train of thought but with less probability for transition to higher states can be extended for $\tau = 0.1 \mu\text{s}$ and $\tau = 1.0 \mu\text{s}$.

We remark for $\tau = 0.1 \mu\text{s}$, $\tau = 1.0 \mu\text{s}$, and $\tau = 10.0 \mu\text{s}$ that around the point $t/\tau \approx 0.8$ the probability of transition to E_1 declines quickly, while the probability of transition to E_2 climbs rapidly. This observation appears probably due to a third minimum energy gap $\Delta E_{\min,21}/h$, which according to Fig. 3.3(b), (d), and (f) occurs near the point $t/\tau \approx 0.8$. This minimum energy gap happens around $t/\tau \approx 0.2$ as well, yet since the state still stays in ground state, no striking rapid drop (increase) for probability of transition to first (second) excited state is observed. This drop or increase could perhaps be observed

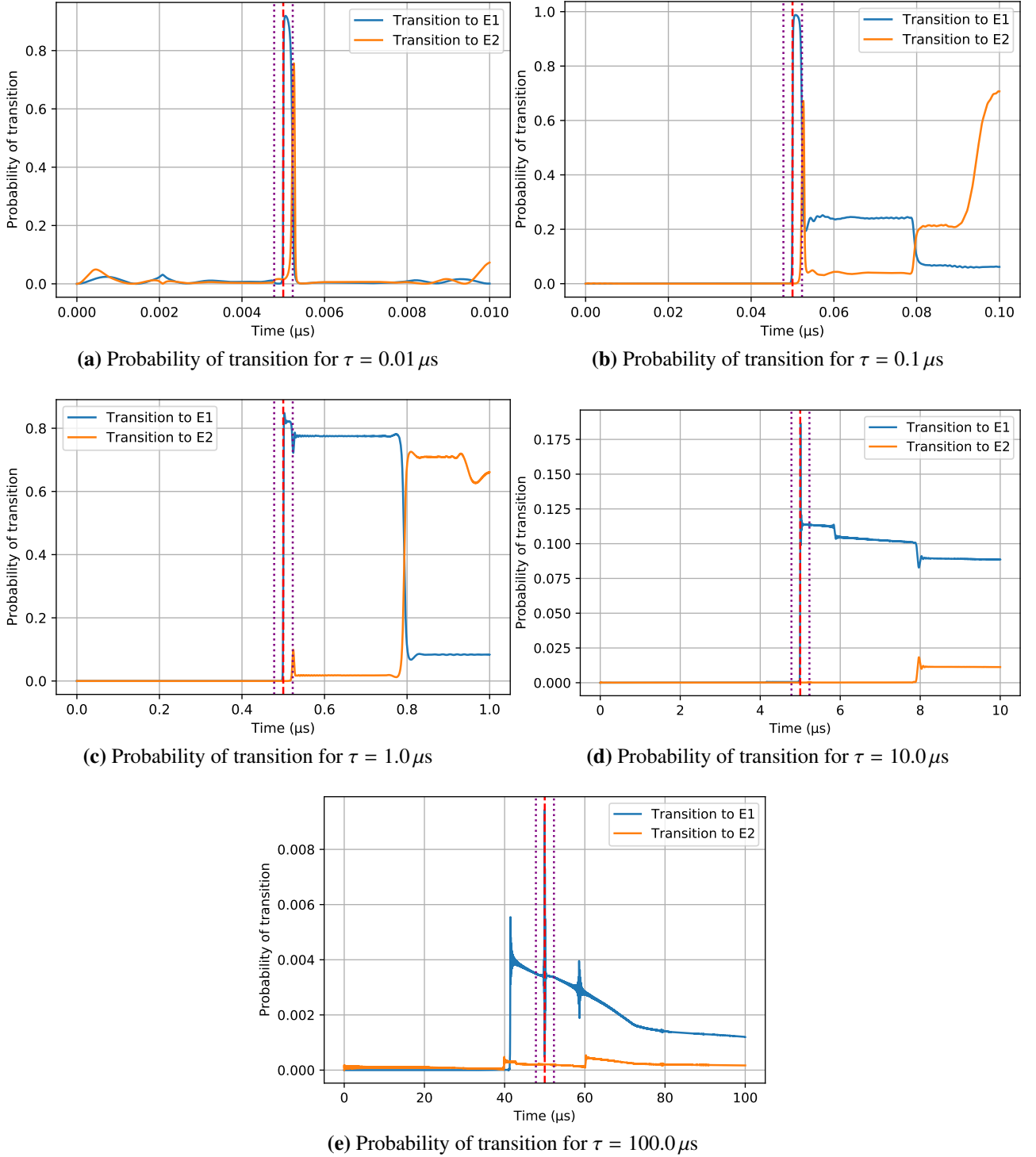
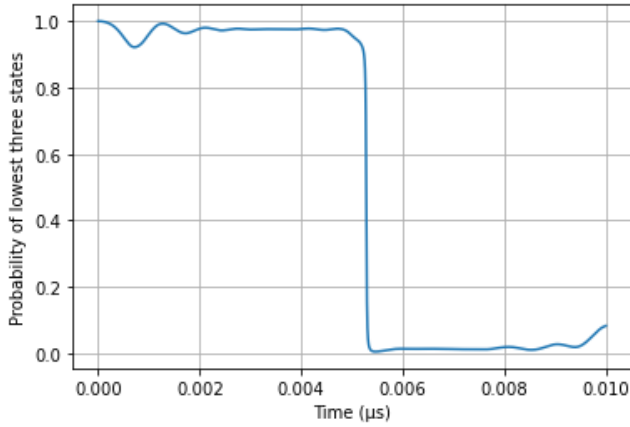
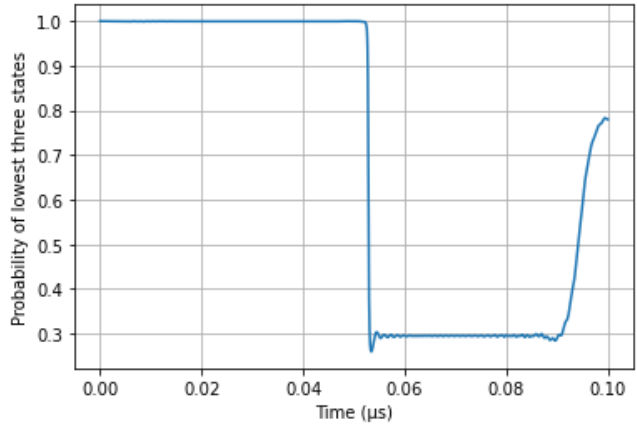


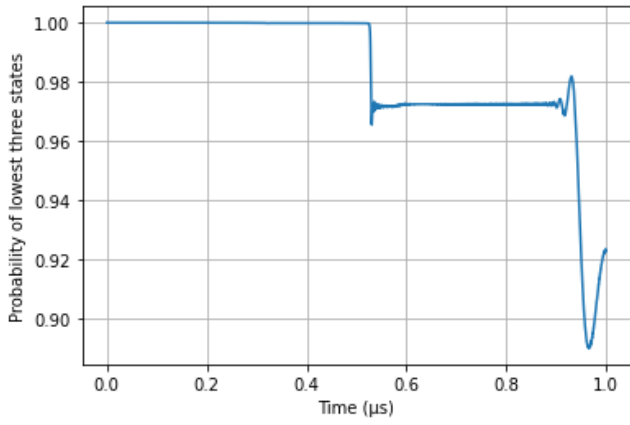
Figure 3.6: Probability of transition to first (second) excited state E_1 (E_2) as a function of time for five different annealing times τ . The red dashed line marks $\Delta E_{\min,10}$ and $\Delta E_{\min,20}$, while the purple dotted line marks $\Delta E_{\min,21}$. The following parameter values: $\forall i \in \{1,2,3,4\} E_{\text{JRM},i}/h = E_{\text{JRM}}/h = 13 \text{ GHz}$, $C_{\text{JRM},i} = C_{\text{JRM}} = 100 \text{ fF}$, $E_{\text{J}1}/h = E_{\text{J}2}/h = 11 \text{ GHz}$, $C_{\text{J}1} = C_{\text{J}2} = 50 \text{ fF}$, and $V_0 = 1.26 \mu\text{V}$ are used.



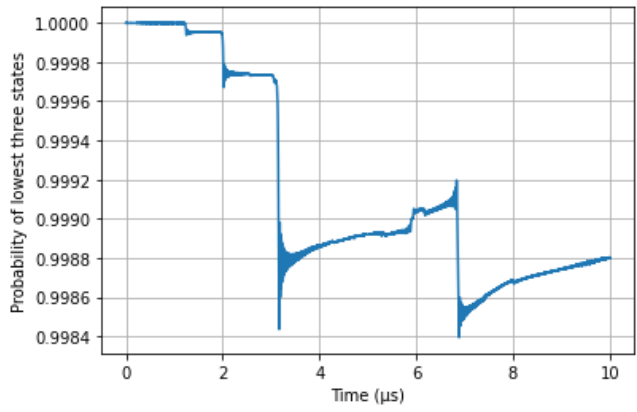
(a) Cumulative probability for $\tau = 0.01 \mu\text{s}$



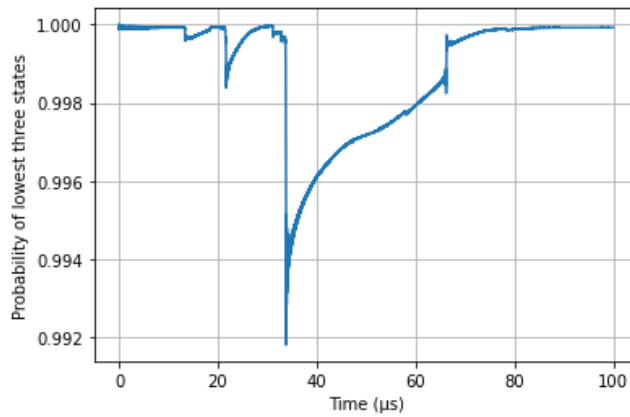
(b) Cumulative probability for $\tau = 0.1 \mu\text{s}$



(c) Cumulative probability for $\tau = 1.0 \mu\text{s}$



(d) Cumulative probability for $\tau = 10.0 \mu\text{s}$



(e) Cumulative probability for $\tau = 100.0 \mu\text{s}$

Figure 3.7: Cumulative probability to find the circuit in either one of three lowest states for five different annealing times τ as a function of time. The following parameter values: $\forall i \in \{1,2,3,4\} E_{\text{JRM},i}/h = E_{\text{JRM}}/h = 13 \text{ GHz}$, $C_{\text{JRM},i} = C_{\text{JRM}} = 100 \text{ fF}$, $E_{\text{J1}}/h = E_{\text{J2}}/h = 11 \text{ GHz}$, $C_{\text{J1}} = C_{\text{J2}} = 50 \text{ fF}$, and $V_0 = 1.26 \mu\text{V}$ are used.

better, if a log scale on y -axis is used.

3.2.2 Parameters Fluctuations

The physical implementation of circuit illustrated in Fig. 3.1 is naturally subject to parameter fluctuations, as every fabrication is always fraught with uncertainties, which might have not been predicted, especially for small parameter magnitude. These uncertainties could eventually change the property and behavior of our circuit during qubit driving, for which reason the final fidelity during the annealing process is investigated under parameter fluctuations. For this purpose, we assume that during fabrication the parameters $E_{\text{JRM},i}$, $C_{\text{JRM},i}$ for $i \in \{1,2,3,4\}$, $E_{\text{J},j}$, $C_{\text{J},j}$ for $j \in \{1,2\}$, and C_k for $k \in \{A,B\}$ deviate at maximum 30% from their intended value. By generating random numbers based on this maximum deviation, we are able to plot the occurrence of final fidelities. Due to non-symmetric parameters, the eigenmodes could deviate from $\tilde{\nu}_1$, $\tilde{\nu}_2$, and $\tilde{\nu}_3$ reported in Subsec. 3.1. To avoid driving error, we adjust manually the initial driving frequencies with corresponding eigenfrequencies of the qubit for each randomly generated parameter set. For this investigation, we set $\tau = 5 \mu\text{s}$ and $V_0 = 1.26 \mu\text{V}$. This procedure yields the results depicted in Fig. 3.8.

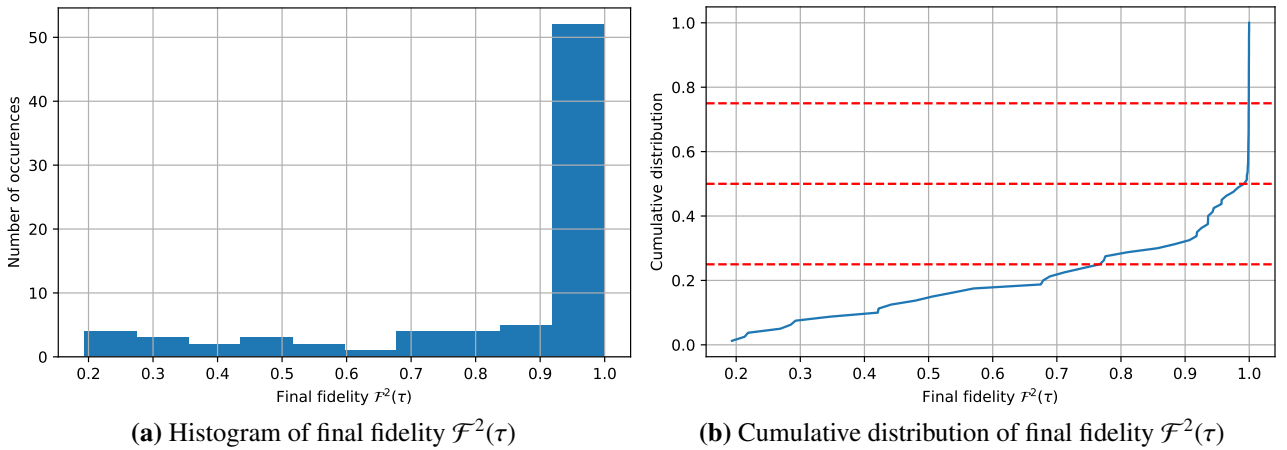


Figure 3.8: Distribution of final fidelities $\mathcal{F}^2(\tau)$ from 80 random parameter sets for $\tau = 5 \mu\text{s}$. The bottom, middle, and top horizontal dashed red line depicted in right figure marks the 25%, 50%, and 75% percentile, respectively. The initial $V_0 = 1.26 \mu\text{V}$ for the annealing protocol is used here.

Figure 3.8(a) shows that most of random parameter sets yield final fidelity with value ranging from around 0.9 to 1.0, which is pretty close to 1.0. The 50% percentile in Fig. 3.8 intersects with the cumulative distribution at $\mathcal{F}^2(\tau) \approx 0.994$. This means that, one expects to attain final fidelity lower and higher than 0.994, each for 50% of the parameter sets. Meanwhile, 25% and 75% percentiles intersect with cumulative distribution around $\mathcal{F}^2(\tau) \approx 0.772$ and $\mathcal{F}^2(\tau) \approx 0.999$, respectively.

3.2.3 Quantum Annealing with Dissipation

In reality, a quantum system always interacts with its environment, as nothing in nature can be perfectly isolated [27]. Consequently, one needs to add an environmental Hamiltonian $\hat{\mathcal{H}}_E$ and the Hamiltonian $\hat{\mathcal{H}}_{SE}$ governing the interaction of the system with its environment [14]. This Hamiltonian is then put into the Schrödinger or von-Neumann equation $\frac{\partial \hat{\rho}_T}{\partial t} = -\frac{i}{\hbar}[\hat{\mathcal{H}}_T, \hat{\rho}_T]$ to obtain the time evolution of total system's state or density operator over time during annealing process [14, 27]. However, the environment typically has much more degrees of freedom than the system of interest, which makes von-Neumann equation solvable only for very limited special cases. As we are only interested in the dynamics of our system, we trace over the environment degrees of freedom to obtain the reduced density matrix of the system $\hat{\rho}(t) = \text{Tr}_E[\hat{\rho}_T]$ [27]. In order to simplify the problem further, the Markovian and Born approximation are made. The first approximation assumes that the time development in the equations of motion for the reduced system density matrix only depends on the present state $\hat{\rho}(t)$, while the latter assumes the separability of the total system $\hat{\rho}_T(t) = \hat{\rho}(t) \otimes \hat{\rho}_E(t)$ [14, 27, 28]. In addition, the rotating wave approximation is performed to neglect all fast rotating terms [28], yielding the Gorini-Kossakowski-Sudarshan-Lindblad or Lindblad equation as follows [28]

$$\frac{\partial \hat{\rho}(t)}{\partial t} = -\frac{i}{\hbar}[\hat{\mathcal{H}}(t), \hat{\rho}(t)] + \sum_k \Gamma_k \left(\hat{L}_k(t) \hat{\rho}(t) \hat{L}_k^\dagger(t) - \frac{1}{2} \{ \hat{L}_k(t) \hat{L}_k^\dagger(t), \hat{\rho}(t) \} \right), \quad (3.16)$$

where \hat{L}_k denotes jump operators, through which the environment couples with the system, and Γ_k are the corresponding rates. The numerical solution of Eq. (3.16) is supported by QuTip.

Due to interaction with environment, our proposed circuit is prone to decay and dephasing phenomena, which cause information loss during annealing time. The first phenomenon describes depolarization along the qubit quantization axis, so that it is often referred to as energy decay. This causes a loss of circuit energy and thus the excitation rate is suppressed exponentially [14]. The latter phenomenon is caused by longitudinal noise that couples to the qubit via the z -axis. This noise causes the qubit frequency to fluctuate such that it is no longer equal to the interaction frame frequency [14]. Due to interaction, qubits generally experience both excitation and relaxation, yet due to Boltzmann statistics and as qubits are usually operated at low temperature ($T \lesssim 20$ mK) with frequencies in the GHz regime, the qubits tend to lose energy to the environment, meaning that the relaxation normally dominates [14]. These two phenomena affect the behavior of our circuit, which in turn motivates this study.

For this study, the decay and dephasing process for $k \in \{1, 2, 3\}$ is introduced via the following jump operators

$$\begin{aligned} \hat{L}_{k,\text{decay}} &= \hat{a}_k, & \Gamma_{k,\text{decay}} &= \frac{2\pi}{T_\gamma}, \\ \hat{L}_{k,\text{dephasing}} &= \hat{a}_k^\dagger \hat{a}_k, & \Gamma_{k,\text{dephasing}} &= \frac{2\pi}{T_\phi}, \end{aligned}$$

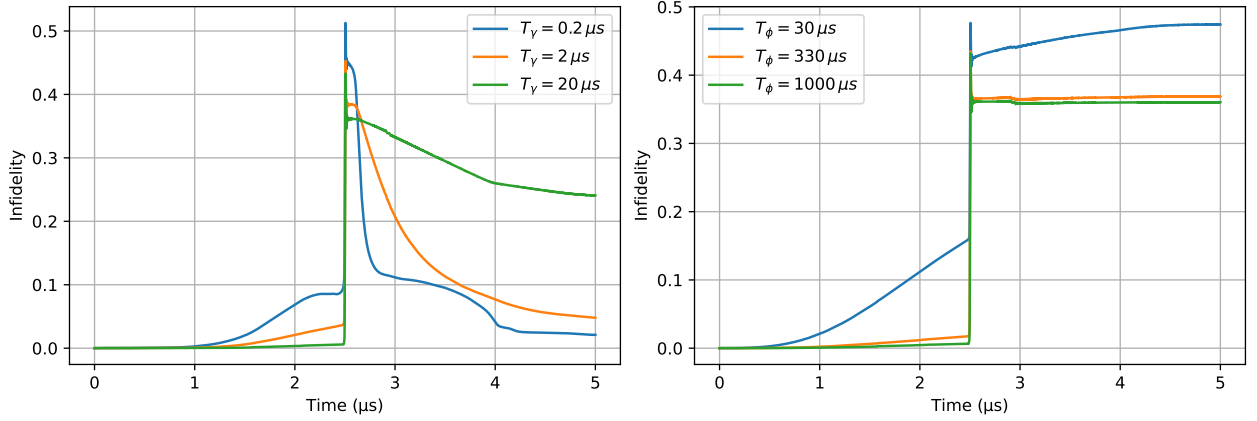
where $\frac{1}{T_\gamma}$ denotes the decay rate of the qubit and $\frac{1}{T_\phi}$ marks the dephasing rate of the qubit. Thus, we

assume equal decay and dephasing rates for each qubit. At first, we want to examine the influence of the decay and dephasing of each qubit on the density operator evolution during annealing protocol. To proceed, we introduce $\hat{L}_{k,\text{decay}}$ or $\hat{L}_{k,\text{dephasing}}$ only for k -qubit of our interest and neglect the interaction of other qubits with the environment. Due to the symmetry of JRM, we introduce the jump operators separately on two qubits, namely qubit associated with Y-eigenmode ($k = 2$) and qubit corresponding to Z-eigenmode ($k = 3$). We remind that qubits associated with X- and Y-eigenmode stem from our two Transmon qubits, which are coupled via JRM, while qubit associated with Z-eigenmode arises from the parasitic capacitance of the Josephson junctions in our JRM, which is also confirmed by Roy [21]. This qubit is coupled as well with the qubit X and Y, as we have the terms g_{j3}^z in Eq. (3.7). Hence, the separate introduction of jump operators $\hat{L}_{3,\text{decay}}$ and $\hat{L}_{3,\text{decoherence}}$ aims to investigate the influence of the interaction between the environment and the qubit associated with Z-eigenmode on the behavior of the whole circuit. For this investigation, we set $\tau = 5 \mu\text{s}$ again. The following parameter values: $\forall i \in \{1,2,3,4\} E_{\text{JRM},i}/h = E_{\text{JRM}}/h = 13 \text{ GHz}$, $C_{\text{JRM},i} = C_{\text{JRM}} = 100 \text{ fF}$, $E_{\text{J1}}/h = E_{\text{J2}}/h = 11 \text{ GHz}$, and $C_{\text{J1}} = C_{\text{J2}} = 50 \text{ fF}$ are used. The result for Y-eigenmode and Z-eigenmode can be seen in Fig. 3.9 and 3.10, respectively.

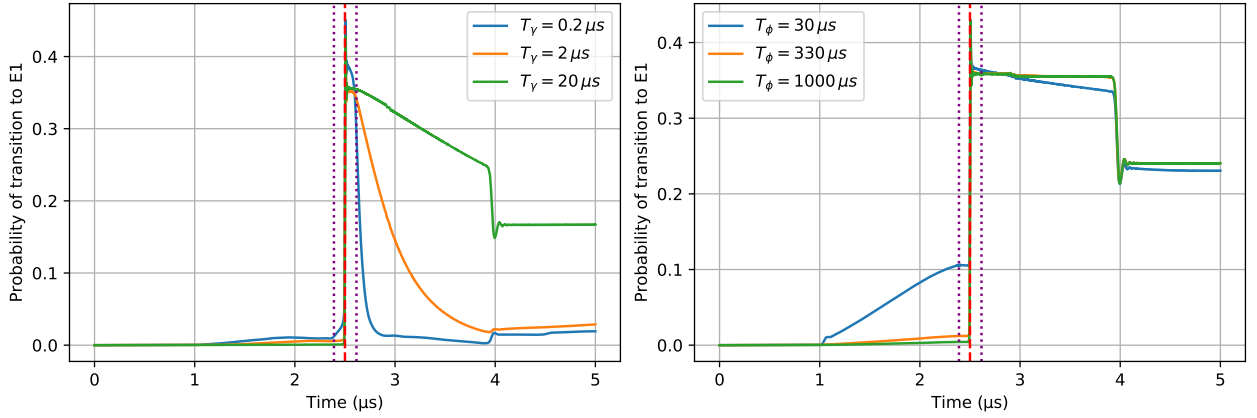
Figure 3.9(a), 3.10(a), 3.9(b), and 3.10(b) show that at the beginning of the annealing protocol, around the third minimum local energy gap $\Delta E_{\text{min},21}/h$ at $t \approx 1 \mu\text{s}$ or somewhat earlier, the infidelity increases steadily, before it rapidly jumps at $t \approx 2.5 \mu\text{s}$, where the minimum energy gap $\Delta E_{\text{min},10}/h$ is reached. In between, the steepness of the infidelity evolution is proportional to the decay rate and dephasing rate. However, after rapid jump at $t \approx 2.5 \mu\text{s}$ the decay jump operator \hat{L}_{decay} has a different influence on the infidelity from the influence of dephasing jump operator $\hat{L}_{\text{dephasing}}$. The first one contributes to the decline of infidelity, whilst the latter slightly affects the growth of infidelity after its rapid drop, especially for $T_\phi = 30 \mu\text{s}$. The decline (increase) of infidelity seems to correspond to the decay (dephasing) rate. From our point of view, the decrease of infidelity is attributed to the annihilation operator \hat{a} , which represents the relaxation of qubits. The relaxation enables the excited state to descend into the ground state and thus suppressing infidelity, whereby the suppression depends positively on the decay rate $\frac{1}{T_\gamma}$. On the other hand, the dephasing jump operator is equal to the number operator $\hat{a}^\dagger \hat{a}$, which corresponds to a dephasing of the off-diagonal elements of the density matrix, a mechanism washing out the phase relationship between states without changing their population [29]. This dephasing effect causes the quantum system to lose its coherence with rate $\frac{1}{T_\phi}$ and thus enhances the infidelity.

This result of course raises a question, whether one can carry out quantum annealing protocol by increasing the decay rate indefinitely. We think, that this possibility is limited, as one needs to cool down the environment further to suppress the excitation of ground state or to increase the decay rate [14]. We hypothesize, that the increase of decay rate is not indefinite with decreasing temperature, but starts to saturate after the environment temperature falls below a certain temperature.

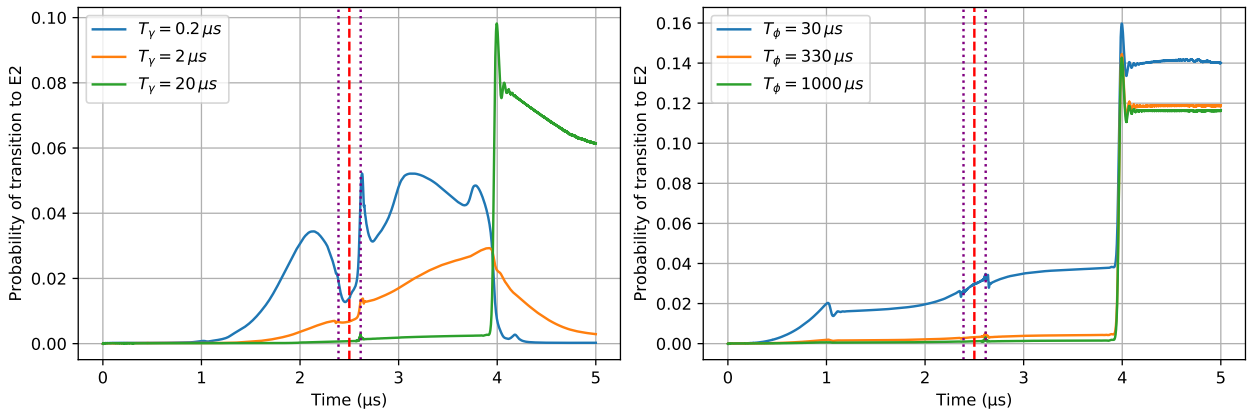
Figure 3.9(c), 3.10(c), 3.9(d), and 3.10(d) depict the transition probability to first excited state, which is distinguished through its rapid jump around $t \approx 2.5 \mu\text{s}$ as similar as Fig. 3.6. After that, the system with



(a) Infidelity of the state for three different decay rates (b) Infidelity of the state for three different dephasing rates

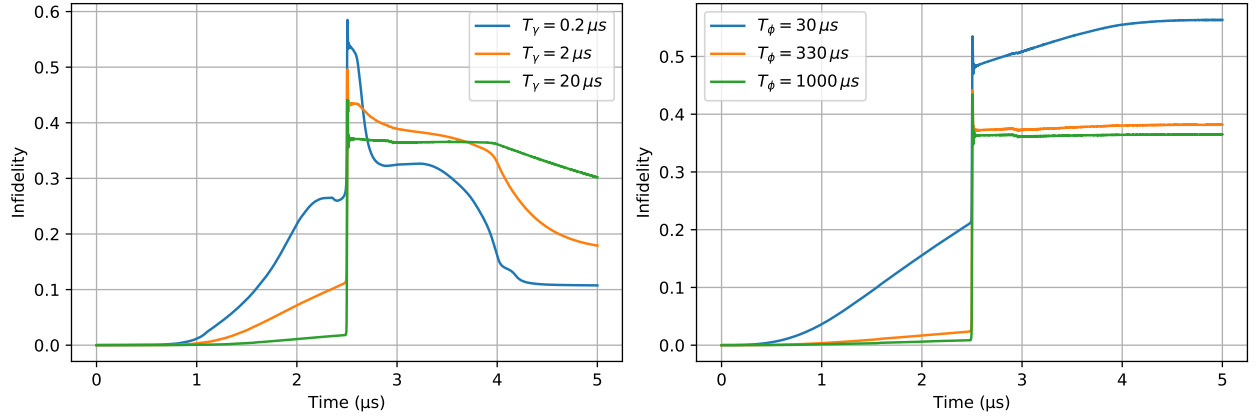


(c) Probability of transition to first excited state for three different decay rates (d) Probability of transition to first excited state for three different dephasing rates

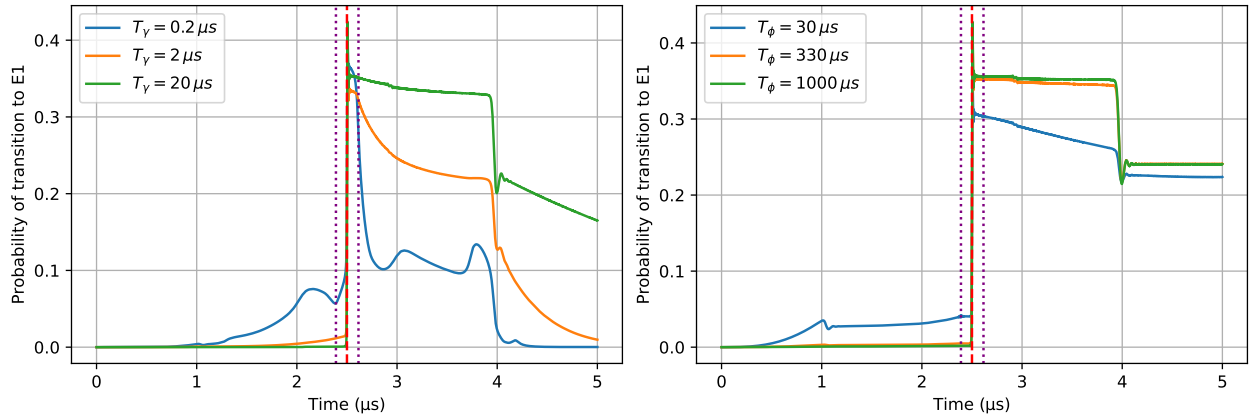


(e) Probability of transition to second excited state for three different decay rates (f) Probability of transition to second excited state for three different dephasing rates

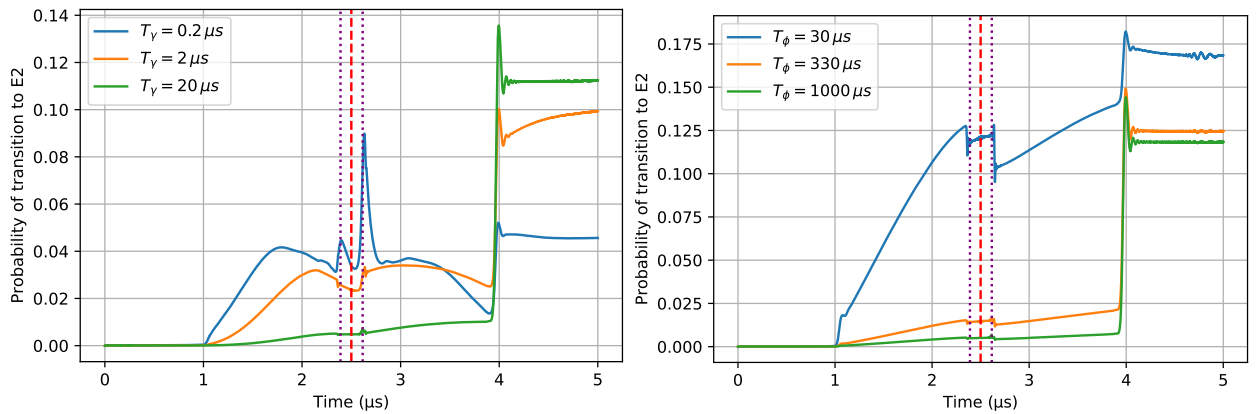
Figure 3.9: Effect of jump operator $\hat{L}_{2,\text{decay}}$ (left) and $\hat{L}_{2,\text{dephasing}}$ (right) of qubit associated with Y-eigenmode on the behavior of circuit's state, plotted as a function of time. The annealing time is set to be $\tau = 5 \mu s$. The red dashed line marks the time point, at which $\Delta E_{\min,10}/h$ and $E_{\min,20}/h$ is reached, whilst the purple dotted line marks the time point of $\Delta E_{\min,21}/h$.



(a) Infidelity of the state for three different decay rates (b) Infidelity of the state for three different dephasing rates



(c) Probability of transition to first excited state for three different decay rates (d) Probability of transition to first excited state for three different dephasing rates



(e) Probability of transition to second excited state for three different decay rates (f) Probability of transition to second excited state for three different dephasing rates

Figure 3.10: Effect of jump operator $\hat{L}_{3,\text{decay}}$ (left) and $\hat{L}_{3,\text{dephasing}}$ (right) of qubit associated with Z-eigenmode on the behavior of circuit's state, plotted as a function of time. The annealing time is set to be $\tau = 5 \mu\text{s}$. The red dashed line marks the time point, at which $\Delta E_{\min,10}/h$ and $E_{\min,20}/h$ is reached, whilst the purple dotted line marks the time point of $\Delta E_{\min,21}/h$.

energy relaxation exhibits a rapid decline of transition probability (see Fig. 3.9(c) and 3.10(c)), whereas a somewhat slower decrease can be seen in Fig. 3.9(d) and 3.10(d) for a system with a dephasing jump operator. In addition, in Fig. 3.9(e), 3.10(e), 3.9(f), and 3.10(f) one can observe a local peak, which is attributed to the local minimum energy gap $\Delta E_{\min,21}/h$. The peak of transition probability to the second excited state is recognized again at $t \approx 4 \mu\text{s}$, where the third minimum energy gap $\Delta E_{\min,21}/h$ around $t/\tau \approx 0.8$ is located. At this time point, the population in first excited state tends to pass over the second excited state.

Since both Fig. 3.9 and Fig. 3.10 show a tendency for the infidelity to increase due to dephasing jump operator, whilst decay jump operator suppresses transition to higher states, one expects both jump operators to compete with each other, when they are simultaneously introduced to the system. Thus, as a last part of this study, we show the time evolution of the circuit state with all its qubits interacting with their surroundings in Fig. 3.11. We assume here, for simplicity, that the decay rate and dephasing rate of all qubits to be equal to each other ($T_{k,\gamma} = T_\gamma$ for $k \in \{1,2,3\}$ and $T_{k,\phi} = T_\phi$ for $k \in \{1,2,3\}$).

As our intuition predicts, the infidelity appears to maximally decline for circuit with large decay rates. Here, the dephasing mechanism has negligible effect on the behavior of circuit state. For smaller decay rates, we observe the infidelity of the state to be somewhat closer to ideal quantum annealing. The largest jump of infidelity appears, again, at $t \approx 2.5 \mu\text{s}$, where $\Delta E_{\min,10}/h$ and $\Delta E_{\min,20}/h$ lay. This time point is characterized by a local peak of transition probability to the first excited state, as observed in Fig. 3.11(b). Shortly after this jump, the infidelity as well as the transition probability to the first excited state drops quickly. This drop is partially attributed to the decay to the ground state and to the excitation to the next higher states, i.e. the second excited state, since local peak in Fig. 3.11(c) intersects with right purple dotted line. Afterwards, around the third local minimum energy gap $\Delta E_{\min,21}/h$ at $t \approx 4 \mu\text{s}$, the transition probability to first excited state decreases, whereas the transition probability to second excited state increases.

Figure 3.11(a) and Figure 3.11(d) illustrate the increase in infidelity and the probability to be in either one of three lowest states. One can recognize that, at the beginning, the circuit interacting with environment exhibits a growing infidelity, even for circuits with high decay rate. This behavior is somewhat counterintuitive and occurs perhaps since both decay and dephasing jump operators negatively affect the adaptability of circuit state during the early phase of annealing protocol. Hence, the probability of being in instantaneous ground state become dispersed over higher states, inferred from the reduction of cumulative probability shown in Fig. 3.11(d).

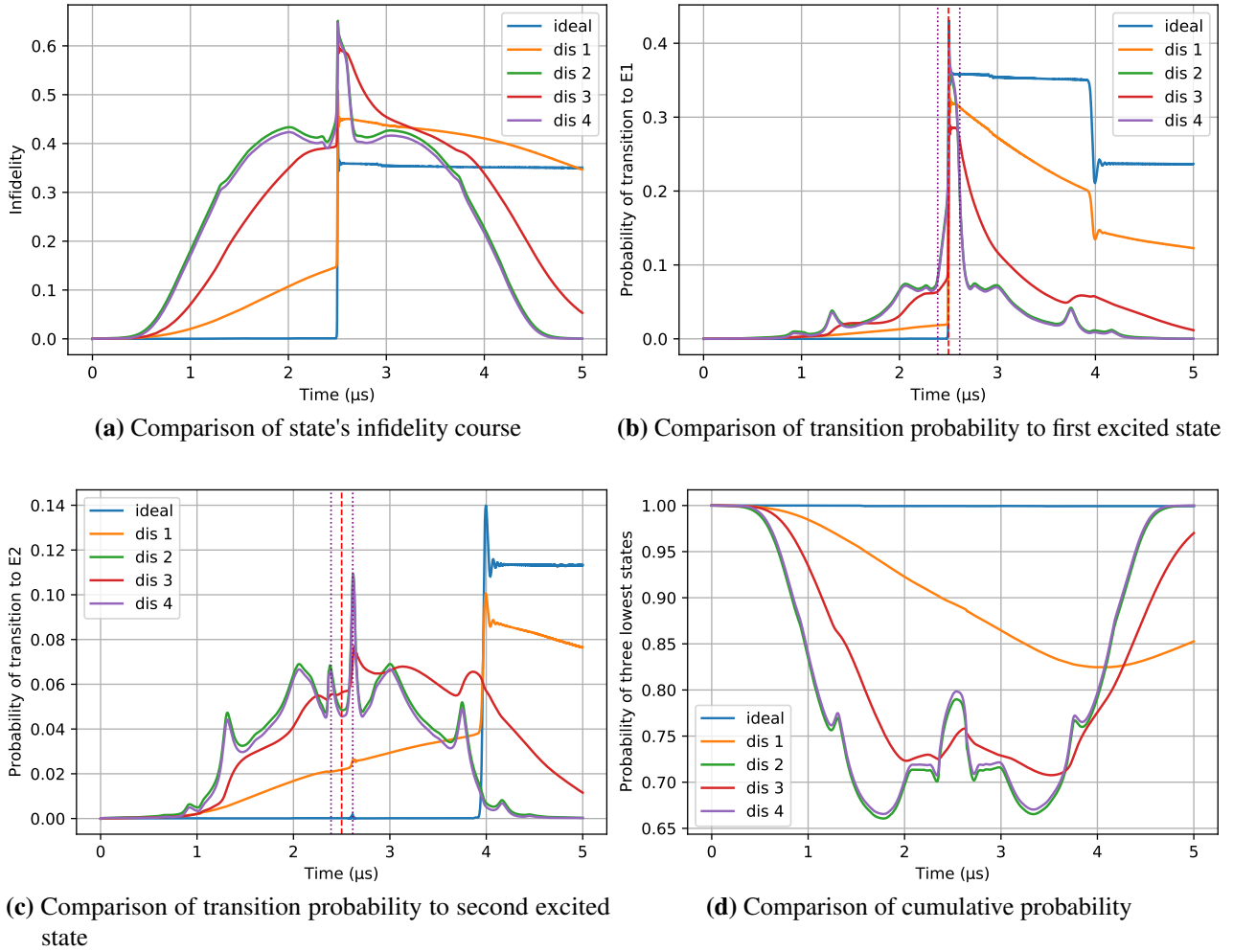


Figure 3.11: The behavior of circuit's state with and without interaction with the environment. "Ideal", "Dis 1", "Dis 2", "Dis 3", and "Dis 4" denote no interaction, $T_\gamma = 20 \mu\text{s}$ and $T_\phi = 330 \mu\text{s}$, $T_\gamma = 0.2 \mu\text{s}$ and $T_\phi = 30 \mu\text{s}$, $T_\gamma = 2 \mu\text{s}$ and $T_\phi = 330 \mu\text{s}$, $T_\gamma = 0.2 \mu\text{s}$ and $T_\phi = 1000 \mu\text{s}$, respectively. The red dashed line marks the time point, at which $\Delta E_{\min,10}/h$ and $E_{\min,20}/h$ is reached, whilst the purple dotted line marks the time point of $\Delta E_{\min,21}/h$.

Chapter 4

Summary and Outlook

We review our main findings once more and highlight several important keynotes of our discussion. In Sec. 3.1 we introduced a coupler circuit based on JRM, and derived its governing Hamiltonian \mathcal{H} by applying electrical network graph theory of Rasmussen [14] and Zlatko [15]. By quantizing the Hamiltonian, we were able to extract essential parameter values and confirmed the analytical expression derived by Leib [13] and Roy [21]. Furthermore, our eigenmode results also coincide with JRM-eigenmodes calculated by Roy [21] and Flurin [22].

Next, in Sec. 3.2 the annealing protocol was investigated. The voltage sources were initially turned on with finite voltage amplitudes and drive frequencies equal to the eigenfrequency of qubit A or B. These initial values were slowly diminished over time. This protocol produced an eigenenergy evolution, from which we extracted the minimum energy gap $\Delta E_{\min,10}/h \approx 165$ MHz and $\Delta E_{\min,20}/h \approx 3.6$ GHz. After that, we studied the influence of the annealing time τ on the infidelity $1 - \mathcal{F}^2(t)$ of our circuit under ideal conditions and fitted an exponential function to the obtained data. This approach yielded the dependency of final infidelity on the annealing time. By this mean, we could confirm the adiabatic theorem, as the final infidelity turns out to be inversely proportional to the annealing time. Besides that, a rapid jump of the final infidelity typically occurs at the time $t/\tau \approx 0.5$ where the system has the minimum energy gap $\Delta E_{\min,10}/h$ and $\Delta E_{\min,20}/h \approx 3.6$ GHz. Moreover, we also tracked the path of the evolving state and found out that the probability of transition to E_1 (E_2) is largest at $\Delta E_{\min,10}$ ($\Delta E_{\min,21}$) for low annealing time. The probability of excitation to energy levels beyond the second excited state is also higher, the shorter the annealing time is. By assuming maximum deviation of a 30% for each component of our circuit from the ideal parameter value, we showed that final fidelities overwhelmingly amounts to 0.9 – 1.0 for $\tau = 5 \mu\text{s}$, indicating robustness of our circuit under fabrication inaccuracies. By introducing the decay jump operator \hat{a}_k with its corresponding decay rate as well as dephasing jump operator $\hat{a}_k^\dagger \hat{a}_k$ with its corresponding dephasing rate, we observed a reduction (slight increase) of the final infidelity for large decay (dephasing) rates. Despite of qubit relaxation, we also observed a reduction of the cumulative probability for circuits with large decay rate, which, from our point of view, is attributed to the worsening of circuit state adaptability during the early phase of the annealing protocol. The reduced adaptability, in turn, causes circuit state to be more dispersed over higher energy levels.

As a closing statement, we would like to mention that this work puts heavy emphasis on numerical solution of the Schrödinger equation and Lindblad equation supported by QuTip. As such, the result is fraught with numerical inaccuracies brought by Python and QuTip. We were, for instance, aware at the end of the work, that there is a discrepancy between Mathematica and Python, which results in different \mathbf{E}^{-1} , the matrix, which expresses Φ_m as a linear combination of twigs Φ_t . Therefore, the eigenmodes $\tilde{\mathbf{v}}_1$ and $\tilde{\mathbf{v}}_2$ computed with Python are not perfectly orthogonal to each other, even though they should be, as the matrix \mathbf{C} and \mathbf{L}^{-1} are positive-definite, real, and symmetric. By manually correcting \mathbf{E} , the minimum energy gap $\Delta E_{\min,10}/h$ approximately doubles, which probably decreases the infidelity even further. Qualitatively, however, the eigenenergy evolution is still highly similar to the eigenenergy evolution without correction. The exact, quantitative consequence of this correction could unfortunately not be investigated due to the limited time frame of this work. Nevertheless, because of the larger energy gap $\Delta E_{\min,10}/h$, we expect the maximum and final infidelity after correction to be *as high as without correction at the most*.

Another conceivable numerical inaccuracy is the annihilation operator \hat{a}_k , which is truncated first and is contained in the non-linear Lagrangian in Eq. (3.4). Due to earlier truncation, the multiplication of \hat{a}_k with itself produces several errors in the matrix entries of $\langle i|\hat{a}_k^2|j\rangle$. To minimize this inaccuracy, we truncated the annihilation operator to the four lowest energy eigenbasis states.

Due to the numerical inaccuracies described above, we advise to investigate the infidelity of our quantum annealing protocol after correction of \mathbf{E}^{-1} and $\langle i|\hat{a}_k^2|j\rangle$. Moreover, a study of state infidelity under parameter fluctuations and jump operators would also be an interesting thing to know, as non-symmetrical circuit interacting with its environment perhaps would behave differently from symmetrical one.

Bibliography

- [1] E. Ilievski. Adiabatic Quantum Computation (University of Ljubljana, 2010).
- [2] A. M. Childs, E. Farhi & J. Preskill. Robustness of adiabatic quantum computation. *Phys. Rev. A* **65**, 012322 (2001).
- [3] J. Paz & W. Zurek. Quantum Limit of Decoherence: Environment Induced Superselection of Energy Eigenstates. *Physical Review Letters* **82**, 5181–5185 (1999).
- [4] S. Lloyd. Robustness of Adiabatic Quantum Computing. [arXiv.0805.2757\[quant-ph\]](#) (2008).
- [5] B. Tamir & E. Cohen. Notes on Adiabatic Quantum Computers. [arXiv.1512.07617\[quant-ph\]](#) (2016).
- [6] W. Lechner, P. Hauke & P. Zoller. A quantum annealing architecture with all-to-all connectivity from local interactions. *Science Advances* **1** (2015).
- [7] H. G. Katzgraber, F. Hamze & R. S. Andrist. Glassy Chimeras Could Be Blind to Quantum Speedup: Designing Better Benchmarks for Quantum Annealing Machines. *Phys. Rev. X* **4**, 021008 (2014).
- [8] T. Jörg, F. Krzakala, J. Kurchan & A. C. Maggs. Simple Glass Models and Their Quantum Annealing. *Phys. Rev. Lett.* **101**, 147204 (2008).
- [9] C. Klymko, B. D. Sullivan & T. S. Humble. Adiabatic quantum programming: minor embedding with hard faults. *Quantum Information Processing* **13**, 709–729 (2014).
- [10] A. Perdomo-Ortiz, N. Dickson, M. Drew-Brook, G. Rose & A. Aspuru-Guzik. Finding low-energy conformations of lattice protein models by quantum annealing. *Scientific Reports* **2**, 571 (2012).
- [11] T. F. Ronnow, Z. Wang, J. Job, S. Boixo, S. V. Isakov, D. Wecker, J. M. Martinis, D. A. Lidar & M. Troyer. Defining and detecting quantum speedup. *Science* **345**, 420–424 (2014).
- [12] D. A. Lidar. Towards Fault Tolerant Adiabatic Quantum Computation. *Phys. Rev. Lett.* **100**, 160506 (2008).

- [13] M. Leib, P. Zoller & W. Lechner. A transmon quantum annealer: decomposing many-body Ising constraints into pair interactions. *Quantum Science and Technology* **1**, 015008 (2016).
- [14] S. E. Rasmussen, K. S. Christensen, S. P. Pedersen, L. B. Kristensen, T. Bækkegaard, N. J. S. Loft & N. T. Zinner. The superconducting circuit companion – an introduction with worked examples. arXiv.2103.01225. [quant-ph] (2021).
- [15] Z. K. Mineev, Z. Leghtas, S. O. Mundhada, L. Christakis, I. M. Pop & M. H. Devoret. Energy-participation quantization of Josephson circuits. arXiv.2010.00620 [quant-ph] (2021).
- [16] S. P. Pedersen, K. S. Christensen & N. T. Zinner. Native three-body interaction in superconducting circuits. *Phys. Rev. Research* **1**, 033123 (2019).
- [17] A. Wallraff, D. I. Schuster, A. Blais, L. Frunzio, R. S. Huang, J. Majer, S. Kumar, S. M. Girvin & R. J. Schoelkopf. Strong coupling of a single photon to a superconducting qubit using circuit quantum electrodynamics. *Nature* **431**, 162–167 (2004).
- [18] J. Koch, T. M. Yu, J. Gambetta, A. A. Houck, D. I. Schuster, J. Majer, A. Blais, M. H. Devoret, S. M. Girvin & R. J. Schoelkopf. Charge-insensitive qubit design derived from the Cooper pair box. *Phys. Rev. A* **76**, 042319 (2007).
- [19] A. A. Houck, J. A. Schreier, B. R. Johnson, J. M. Chow, J. Koch, J. M. Gambetta, D. I. Schuster, L. Frunzio, M. H. Devoret, S. M. Girvin & R. J. Schoelkopf. Controlling the Spontaneous Emission of a Superconducting Transmon Qubit. *Phys. Rev. Lett.* **101**, 080502 (2008).
- [20] R. Barends, J. Kelly, A. Megrant, D. Sank, E. Jeffrey, Y. Chen, Y. Yin, B. Chiaro, J. Mutus, C. Neill & et al. Coherent Josephson Qubit Suitable for Scalable Quantum Integrated Circuits. *Phys. Rev. Lett.* **111**, 080502 (2013).
- [21] T. Roy. *Multimode Superconducting Circuits as Building Blocks for a Programmable Quantum Processor*. Ph.D. thesis, Department of Condensed Matter Physics and Materials Science Tata Institute of Fundamental Research, Mumbai (2018).
- [22] E. Flurin. *The Josephson mixer : A Swiss army knife for microwave quantum optics*. Ph.D. thesis, Department of Physics, École Normale Supérieure (2014).
- [23] J. Johansson, P. Nation & F. Nori. QuTiP: An open-source Python framework for the dynamics of open quantum systems. *Computer Physics Communications* **183**, 1760–1772 (2012).
- [24] J. Johansson, P. Nation & F. Nori. QuTiP 2: A Python framework for the dynamics of open quantum systems. *Computer Physics Communications* **184**, 1234–1240 (2013).

- [25] E. Farhi, J. Goldstone, S. Gutmann & M. Sipser. Quantum Computation by Adiabatic Evolution. [arXiv.0001106](https://arxiv.org/abs/quant-ph/0001106). [quant-ph] (2000).
- [26] C. Wittig. The Landau-Zener Formula. *J. Phys. Chem. B* **109**, 8428–8430 (2005).
- [27] D. Manzano. A short introduction to the Lindblad master equation. *AIP Advances* **10**, 025106 (2020).
- [28] D. Manzano & P. Hurtado. Harnessing symmetry to control quantum transport. *Advances in Physics* **67**, 1 – 67 (2017).
- [29] F. Laussy, E. Del Valle, T. U. München, A. Laucht, A. Gonzalez-Tudela, M. Kaniber, J. Finley & C. Tejedor. 9 - Luminescence spectra of quantum dots in microcavities. In *Quantum Optics with Semiconductor Nanostructures* Woodhead Publishing Series in Electronic and Optical Materials (ed. F. Jahnke) 293–331 (Woodhead Publishing, 2012).

Acknowledgement

At the end of this work, I would like to express my gratitude to all the people who have supported me during my whole bachelor study and who have contributed to the completion of this thesis.

First, I am thankful to **Dr. rer. nat. Frank Deppe**, for allowing me to write my bachelor thesis with this exciting topic at the Walther-Meißner-Institute. He is an attentive reader and always gave me highly constructive feedbacks, which help me increase the quality of this thesis.

Second, I express my gratitude to **Yuki Nojiri, M.Sc.** for his introduction to this fascinating quantum computing research field and for his great patience in guiding me and answering my repeating questions. My discussion with him was always fruitful and his feedbacks contributed substantially to this thesis. I hope that this humble work could help him pursuing his Ph.D. program.

Next, I owe **Hisyam Attamimi Zain** a lot for his willingness to provide me his powerful PC. Without his PC, I might not finish my thesis punctually or would have to be content with less scope of study, as the whole simulation would take much longer time.

After that, I thank my fellow students **Cenanda Ra'ifanarido** and **Vernando Fransiscus Limodya**, for our study time together. Without them, I would have to put more endeavors during my whole bachelor study in physics and the whole program would be less exciting.

Last but not least, I want to thank my parents, **Muhammad Ridwan** and **Ardiani Ika Sulistyawati**, for giving me the opportunity to study physics and always supporting me during both low and high phase of my life.